Excitonic Coupling on Heliobacterial Symmetrical Type-I Reaction Center: Comparison with Photosystem I

Hirotaka Kitoh-Nishioka,[*,†,‡] Yasuteru Shigeta,[‡] Shigeru Itoh,[¶] and Akihiro Kimura[*,¶]

†*JST, PRESTO, 4-1-8 Honcho, Kawaguchi, Saitama 332-0012, Japan*

‡*Center for Computational Sciences, University of Tsukuba, 1-1-1 Tennodai, Tsukuba, Ibaraki 305-8571, Japan*

¶*Department of Physics, Graduate School of Science, Nagoya University, Furo-cho, Chikusa-ku, Nagoya 464-8602, Japan*

E-mail: hkito@ccs.tsukuba.ac.jp; akimura@tb.phys.nagoya-u.ac.jp

Phone: +81 52 789 2873. Fax: +81 52 789 2873

Abstract

The excitonic couplings among 54 bacteriochlorophylls-g (BChl)-g, 4 BChl-g' and 2 Chl-a_{F} pigments were calculated in the type-I homodimeric reaction center of *Heliobacterium modesticaldum* (hRC), and compared with that in photosystem I (PSI) type-I heterodimeric reaction center. The advanced combination of transition charge of electrostatic-potential with the Poisson equation (Poisson-TrESP), applied for the first time to the excitonic coupling calculation, gave a reliable model in contrast to a model calculated by simple standard dipole-dipole interaction approximation that was qualitatively valid for hRC but not for PSI. The simplest method for the calculation of the long-range contribution to the excitonic coupling on RCs is shown to be the TrESP method, which considers the distance- and orientation-independent local field/screening correction factor. The excitonic couplings of the special pairs, P800 in hRC and P700 in PSI, are also calculated by the fragment excitation difference (FED) scheme at the configuration-interaction singles level, which considers the charge-transfer characteristics of the relevant excitonic states. The calculation realized the reported parameter values for P800 and P700 better than the Poisson-TrESP calculation. Virtual exchanges between Chl-a and BChl-g on hRC and PSI indicated that the difference between hRC and PSI arises from the different electronic-structures of Chl-a and BChl-g pigments themselves and the different arrangements on hRC and PSI. The contributions of excitonic couplings to the functional properties and evolutionary modifications of hRC and PSI are also discussed.

INTRODUCTION

The photon energy absorbed by chlorophyll (Chl) pigments in light-harvesting antenna systems of photosynthetic organisms is efficiently transferred to a special pair or monomer of Chl in the core of the reaction center (RC) pigment-protein complex, and then, induces a charge separation across the membrane. Excitation energy transfer (EET) and electron transfer (ET) on RCs are highly optimized to enable the efficient solar energy conversion

via modifications of proteins and pigments. A recent study has revealed the structure of RC (hRC) of *Heliobacteria*[1] that has long been unknown and hRC has been assumed to be a primitive type-I RC, established in the early stages of the evolution of life. hRC has a unique symmetrical structure unlike all the other RCs, although the currently available hRC structure[1] lacks menaquinone electron acceptor that is predicted to function as the primary electron acceptor[2] phylloquinone (A1) in plant type-I RC photosystem I (PSI).

Photosynthetic RCs can be classified into two types in terms of their structures and terminal electron acceptors: [4Fe–4S]-type iron sulfur clusters work in all type-I RCs and quinones works in all type-II RCs. Oxygenic photosynthesis of plants and cyanobacteria use the linear combination of PSI and PSII to undergo electron transfer from H_2O to $NADPH_2$ PSI complex is a heterodimer of PsaA and PsaB polypeptides and binds 95 Chl-*a*, 1 Chl-*a*', and 22 β-carotenes. PSII is also a heterodimeric RC that binds about 30 Chl-*a*. Anoxygenic photosynthetic purple photosynthetic bacteria uses only type-II RC (designated as pRC hereafter), which is a heterodimer of two partially homologous subunit proteins L and M, and resembles the central moiety of PSII. Another anerobic group of photosynthetic bacteria has type-I homodimeric RCs; hRC of *Heliobacteria*,[3] gRC of green sulfur bacteria,[4] and RC of chloracidobacteria,[5] all of them are homodimers made of two identical subunit proteins and have been assumed to contain symmetrical arrangements of pigments.

Information for the structure of type-I homodimeric RCs has long been unavailable until the 2017 report by Gisriel et al. of the X-ray structure of hRC of *Heliobacterium (Hbt.) modesticaldum* at a 2.2 Å resolution.[1] The structure has a two-fold rotational symmetry made of two PshA subunits (with a small PshX subunit) and contains 54 bacteriochlorophyll *g* (BChl-*g*): 4 BChl-*g*' (a stereoisomer of BChl-*g* at the 13^2 position of ring III), two 8^1-hydroxy-Chl *a* (Chl-a_F), two carotenoids, and an iron–sulfur cluster F_X. Figure 1 illustrates the chemical structures of BChl-*g* and Chl-*a*, and the arrangement of BChls in hRC. The amino acid sequence of PshA has a low but appreciable homology (ca. 30%) to those of PsaA and PsaB of PSI.[3] As shown in Figure 1(e), the arrangement of BChl-*g* on hRC partially

overlaps with that of Chl-*a* on PSI, though hRC has the smaller number of BChl-*g* compared to Chl-*a* on PSI.

It should be also noted that *Hbt. modesticaldum*, which live in strictly anaerobic low-light habitats is known to have the simplest photosynthetic system made of only hRC with no light-harvesting antenna complexes. Both the light-harvesting and charge-separation activities are, therefore, performed on hRC. Though not many studies have been worked on the structure and function of hRC,[2,6–16] laser spectroscopy study of hRC in the isolated membranes under anaerobic condition demonstrated the rapid EETs that complete within 1 ps, suggesting the strong excitonic interaction in hRC.[9] The absorption spectra of hRC by experiment at low temperature[9] is shown in Figure 2.

We proposed the exciton state model on hRC based on the Redfield exciton relaxation theory using the pigment arrangement on hRC with a simple excitonic Hamiltonian.[17] by assuming, rather artificially, a constant site energy value for all BChl-*g* molecule as the first approach. The excitonic couplings among the pigments on hRC were obtained from the dipole–dipole (dd) interactions according to the original Förster theory.[18] Surprisingly, the simple model, even with the assumption of constant site energies for chlorophyll binding sites, reproduced the EET dynamics detected by the laser spectroscopy well, as well as the low/room temperature absorption spectra[9] of hRC as shown in Figure 2. It is indicated that the physical property of hRC is somewhat different from PSI, in which such simple analyses were inapplicable.[17] Chl-*a* which has the weaker transition dipole moments (TDM) than BChl-*g*, was assumed to give different exciton couplings, even on the structure similar to that of hRC. We tested the "pigment replacement analysis" on the hRC and PSI models to study the origin and evolution of the light-harvesting processes in different RCs.[17]

The dd-interaction approximation previously used,[17] is known to break down sometimes for calculation of Förster-type Coulomb couplings, even at intermediate molecular separations[20,21] because the excitonic couplings for EETs is known to arise from the two mechanisms: Förster-type Coulomb coupling mechanism and a short-range coupling mechanism

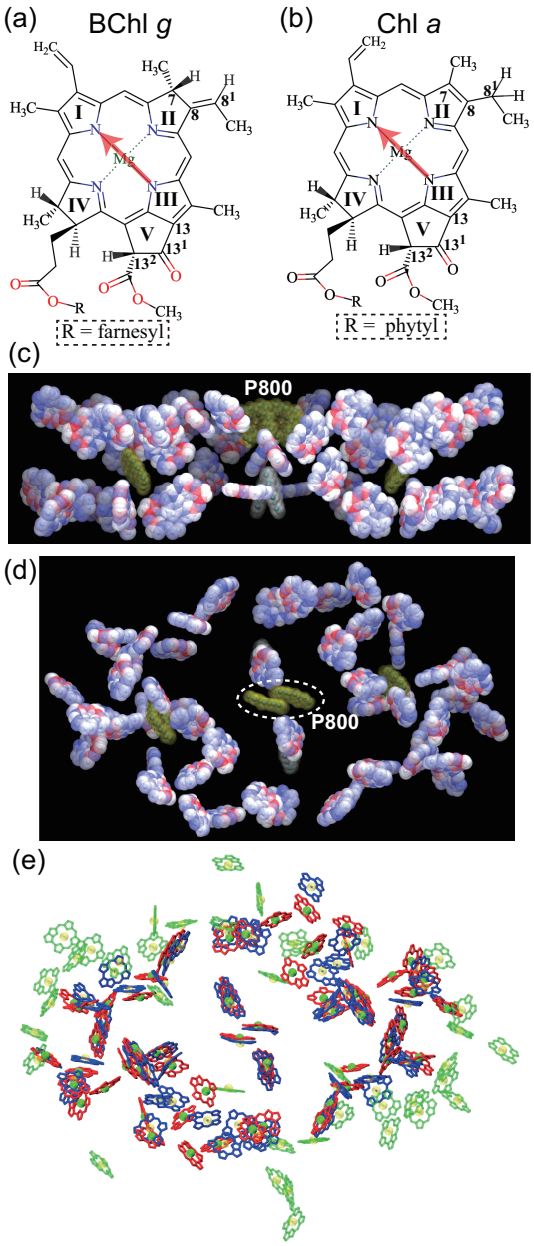

Figure 1: Chemical structures of (a) BChl-g and (b) Chl-a. The direction of TDM used for each pigment is illustrated by a transparent red arrow. Schematic representation of the dielectric volume in the Poisson-TrESP calculations for hRC as viewed from (c) the top of membrane or (d) as a cross section along the membrane normal. (e) Superposition of the pigment arrangement in hRC (solid red sticks) with that in PSI (solid blue sticks for PSI-core and transparent green sticks for the other pigments).

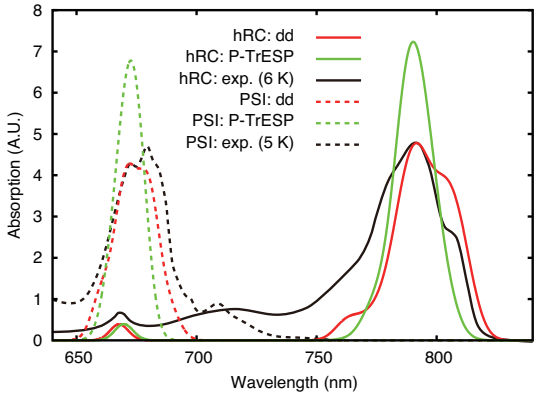

Figure 2: Absorption spectra of hRC and PSI calculated by two models. Red and red-dotted curves represent the numerical results for hRC and PSI calculated by simple dd models.[17] Green and green-dotted curves are calculated by Poisson-TrESP models. Black and black-dotted curves represent the spectra of hRC and PSI experimentally obtained at cryogenic temperature (hRC at 6 K: Neerken et al.[9] PSI at 5 K: Byrdin et al.[19]). Note that calculations are performed at constant site energies for BChl-g or Chl-a. See discussion section for details.

that includes the Dexter-type exchange-coupling mechanism. The difference between Förster and Dexter mechanisms has long been recognized. In general, the Förster-type Coulomb coupling mechanism dominantly works in photosynthetic systems. The methods, more accurate than the dd-interaction method, have been developed for the study of photosynthetic systems.[22–36] Among them, the transition charge from electrostatic potentials (TrESP) method offers an adequate balance between accuracy and computational costs for the excitonic coupling calculations.[32,33] Kenny and Kassal have recently reported the systematic benchmark calculations of excitonic couplings between BChls.[37] Moreover, the combination of the TrESP and Poisson equation, called Poisson-TrESP,[38] can include the influence of the dielectric protein and solvent surrounding the antenna pigments on the excitonic couplings. The Poisson-TrESP method has been applied to many systems.[38–47] In particular, Adolphs et al.[39] have shown that the dd-interaction method is inapplicable to a large number of closely spaced Chl-a molecules in PSI by the analysis using the Poisson-TrESP method. These results question the conclusion of our previous hRC study[17] done simply with the dd-interaction method so that we here carefully calculate the excitonic-couplings in hRC by Poisson-TrESP method and compared hRC and PSI. Evaluation of contribution of site energy for each pigment,

which is also important for the estimation of excitonic states, will be reported elsewhere (in preparation).

Specific excitonic-couplings at short-rages should also be considered in the case of the special pair P800 of hRC. Madjet et al.[48] have reported that this mechanism dominantly contributes to the excitonic coupling of the P700 of PSI by using the energy difference of the two (adiabatic-) excitonic states within an effective two-state approximation. Yin et al.[49] have also calculated the short-range and long-range excitonic couplings of P700 with an effective two-state approximation. We hence calculate the excitonic couplings of the model molecules of the P800 and P700 with the closely related fragment excitation difference (FED)[50] and Edmiston–Ruedenberg localized diabatization (ER-D)[51,52] schemes in this study. Kenny and Kassal[37] recently pointed out that FED method based on the two-state approximation is invalid for the special pairs because the charge-transfer (CT) excited states are significantly mixed with the (Frenkel) exciton states in the two (adiabatic-)excitonic states of BChl dimers (P800) at small intermolecular separations (around 4 Å). Therefore, we analyzed the CT natures of the two adiabatic excited states of P800 and P700 with the descriptor developed by Plasser and Lischka[53] based on the corresponding one-electron transition density matrices.

In this study, we firstly apply the Poisson-TrESP method to the calculation of the Förster-type Coulomb couplings on hRC. We analyze the excitonic coupling of P800 in hRC by using the FED and ER-D schemes. We use numerical results for PSI as a benchmark, and discuss the accuracy of the numerical results in hRC. We discuss the features of the calculated excitonic couplings in hRC protein and compare them with those in the PSI, and re-evaluate the previous dd-interaction approximation result too. We focus on two factors: pigment arrangements on hRC/PSI and the transition density/charges on each BChl-g/Chl-a pigment in hRC/PSI, and will discuss properties of optical spectra and functional relation between hRC and PSI in the evolution of RCs.

COMPUTATIONAL DETAILS

Systems for Förster-Type Coulomb Coupling

We prepared the coordinates of the heavy atoms of 54 BChl-g, 4 BChl-g', and 2 Chl-a_{F} by using the crystal structure of hRC[1] (PDB data 5V8K) with a C_2-symmetric transformation, as plotted in Figure 1(c)–(d). Similarly, the coordinates of the heavy atoms of 95 Chl-a and 1 Chl-a', which were taken from the crystal structure of PSI monomer[54] (PDB data 1JB0) and Ref. 48, respectively, were used for the calculations of Förster-type Coulomb couplings in PSI. It is unknown whether hRCs are aggregated or interacting each other *in vivo*. Therefore, we treated hRC as a monomer in the present study and compared with PSI-monomer rather than PSI-trimer, which was fully reproduced numerically by Adolphs et al..[39] Hereafter, the PSI monomer is just called PSI.

Förster-Type Coulomb Coupling

The Förster-type Coulomb coupling $V_{m,n}$ between mth and nth pigments in the gas phase is expressed by the Coulomb interaction between their one-electron transition densities, as follows:[55–58]

$$V_{m,n} = \int \mathrm{d}\mathbf{r}_1 \int \mathrm{d}\mathbf{r}_2 \frac{\rho_m^{\mathrm{eg}*}(\mathbf{r}_1)\rho_n^{\mathrm{eg}}(\mathbf{r}_2)}{|\mathbf{r}_1 - \mathbf{r}_2|}, \tag{1}$$

where ρ_m^{eg} and ρ_n^{eg} are the transition densities of mth and nth pigments, respectively. This study applied the Poisson-TrESP method to approximate the the Förster-type Coulomb coupling in addition to the simpler conventional dd-interaction method used in the previous study.

Dipole–Dipole Interaction Method

According to the original Förster theory,[18] Eq. 1 is approximated as a dd interaction between transition dipole moments (TDMs) of mth and nth pigments;

$$V_{m,n}^{\mathrm{dd}} = f^{\mathrm{dd}} \frac{1}{4\pi\epsilon_0} \frac{\kappa_{m,n}\mu_m\mu_n}{R_{m,n}^3}, \tag{2}$$

where $R_{m,n}$ is a center-to-center distance between the mth and nth pigments. ϵ_0 is the vacuum permittivity constant. μ_m is an amplitude of the TDM of mth pigment in the gas phase. $\kappa_{m,n}$ is an orientation factor expressed as;

$$\kappa_{m,n} = \hat{\mu}_m \cdot \hat{\mu}_n - 3(\hat{\mu}_m \cdot \hat{\mathbf{R}}_{m,n})(\hat{\mu}_n \cdot \hat{\mathbf{R}}_{m,n}), \tag{3}$$

where the hat $\hat{}$ represents a unit vector. f in Eq. 2 is a factor that takes local field and screening effects into account in an approximate way.[18,39]

For the application of Eq. 2 to the couplings in hRC and PSI, this study adopts the same procedure used in our previous paper.[17] $R_{m,n}$ is calculated from the Mg-to-Mg distance between the mth and nth pigments. μ_m for BChl-g and BChl-g' is set to 6.5 Debye.[59] On the other hand, μ_m for Chl-a, Chl-a', and Chl-a_{F} is set to 4.6 Debye.[59] The direction of $\hat{\mu}_m$ is defined from the distance vector between the positions of NB and ND of the mth pigment. All the coordinates of Mg, NB, and ND atoms of the pigments in hRC and PSI were determined from the corresponding X-ray crystal structures.

Poisson-TrESP Method

TrESP method[32] approximates Eq. 1 as classical Coulomb interaction between atom-centered "transition" charges of mth and nth pigments as;

$$V_{m,n}^{\mathrm{TrESP}} = \sum_I \sum_J \frac{q_I^{(m)} q_J^{(n)}}{|\mathbf{R}_I^{(m)} - \mathbf{R}_J^{(n)}|}, \tag{4}$$

where the $\mathbf{R}_I^{(m)}$ represents the Ith atomic coordinate of the mth pigment prepared from the X-ray structures. We obtain a set of the TrESP charges of mth pigment, $\left\{q_I^{(m)}\right\}$, by a fit of the three-dimensional (3D) "pseudo-ESP" arising from ρ_m^{eg}. Note that the net transition charge is always zero as $\sum_I q_I^{(m)} = 0$, because of the orthogonality between the ground and excited state wave functions.

The Poisson-TrESP method[38–40] can account for the effects of dielectric medium on the Coulomb interaction with the transition charges. The pseudo-ESP arising from the transition charges of mth pigment, $\phi_m(\mathbf{r})$, is first numerically solved by using the following Poisson equation:

$$\nabla \cdot [\epsilon_{\mathrm{opt}}(\mathbf{r}) \nabla \phi_m(\mathbf{r}))] = -4\pi \sum_I q_I^{(m)} \delta^3 \left(\mathbf{r} - \mathbf{R}_I^{(\mathrm{m})}\right), \tag{5}$$

where $\epsilon_{\mathrm{opt}}(\mathbf{r})$ is the optical dielectric constant

$$\epsilon_{\mathrm{opt}}(\mathbf{r}) = \begin{cases} \epsilon_0 & (\mathbf{r} \in (\text{any pigment})) \\ \epsilon & (\mathbf{r} \notin (\text{any pigment})) \end{cases}. \tag{6}$$

The parameter ϵ is the optical dielectric constant. We use $\epsilon = 2$ in the protein with dielectric continuum treatment,[60] and $\epsilon = \epsilon_0 = 1$ in the vacuum.

Then, the excitonic coupling between mth and nth pigments is determined by

$$V_{m,n}^{\mathrm{P-TrESP}} = \sum_J \phi_m \left(\mathbf{R}_J^{(\mathrm{n})}\right) q_J^{(n)}. \tag{7}$$

To calculate the transition charges for the pigments in hRC and PSI, we first prepared the model molecules. Each (bacterio)chlorophyll molecule, in which the farnesyl/phytyl tail is truncated and capped with a methyl group, is considered a pigment model. Then, we performed the ground-state (GS) geometry optimizations on the five pigment models, including BChl-g, BChl-g', Chl-a_{F}, Chl-a, and Chl-a', in the gas phase, using global hybrid B3LYP functional[61] with Grimme empirical dispersion correction D3 and Becke–Johnson

damping (B3LYP-D3BJ).[62] All the geometry optimizations were performed using the cc-pVDZ basis sets[63] with the Gaussian 09 Revision E.01 suite of programs.[64] The coordinates of the model molecules obtained from the geometry optimizations are listed in Tables S1–S5 of Supporting Information.

After the geometry optimizations of the prepared model molecule, we performed the TD-CAM-B3LYP calculation[65] for the first-excited Q_y state of each pigment model using the GAMESS program[66] and the cc-pVDZ basis sets. The TrESP charges, $q_I^{(m)}$'s, are evaluated by fitting to the 3D pseudo-ESP arising from the resultant ρ_m^{eg} on grid points surrounding the model molecule. We generated 10 layers of grid points for each model pigment, starting from 1.4 times the van der Waals radii (vdWR_I) of the atoms, with an even increment of 0.2, using Connolly's molecular surface code implemented in GAMESS. Then, we determine the TrESP charges of the heavy atoms of the model pigments using RESP[67] program in the AmberTools suite package.[68] Note that we constrain all hydrogen atoms to have no charge during the RESP procedure (as with united atom models). As with Refs. 32 and 39, we finally rescale the resultant TrESP charges by the ratio of the experimental to calculated strength of the vacuum transition dipole moment for each pigment model. We adopt 6.5 Debye[59] as the experimental strength of the TDMs of BChl-*a* and BChl-*a*' for the scaling. Similarly, we adopt 4.6 Debye[59] as the experimental strength of the TDMs of Chl-*a*, Chl-*a*', and Chl-a_{F} for the scaling.

Adaptive Poisson-Boltzmann Solver (APBS) version 1.4.2[69] was used with the Poisson-TrESP method. When using Eq. 5, we set $\epsilon_{\mathrm{opt}}(\mathbf{r})$ to 1 where the $\mathbf{r}$ points into the pigment-model cavity consisting of the spheres with simple United Atom Topological Model (UA0) for the atomic radii and is set to 2,[39] where the $\mathbf{r}$ indicates the position of the protein or solvent. The atomic radii of the model molecules used for the calculations are listed in Tables S6–S10 of Supporting Information. Section S3 in Supporting Information explains the details of the computational settings for APBS software.

Short-Range Excitonic Couplings of P800 and P700 Models

For calculating the short-range excitonic couplings of the special pairs P800 (BChl-g'/BChl-g' homo-dimer) in hRC and P700 (Chl-a/Chl-a' hetero-dimer) in PSI, we constructed their model molecules from the similar procedure to Ref. 48 and explain their details in Sec. S4 in Supporting Information. Tables S11 and S12 in Supporting Information list their coordinates.

This study employs the three methods as *ab initio* Frenkel-Davydov exciton model (AIFDEM),[70,71] FED,[50] and ER-D[51,52] schemes. Because the AIFDEM scheme is based on the two (quasi-)diabatic states constructed from the local excitation on each isolated monomer of the special pair, the CT state are not involved in excitonic coupling calculations. On the other hand, because FED and ER-D schemes are based on the two adiabatic excitonic states, one needs to pay attention to the CT-state contamination in excitonic coupling calculations.[37]

For all the short-range excitonic-coupling calculations, this study used the 6-31G(d) basis sets. Although the P800 model has a C_2 molecular symmetry, it was disabled for all the calculations.

AIFDEM Scheme

We regard the special-pair model as a system of two chromophores, A and B, and difine two (quasi-)diabatic electronic states by $|A^*B\rangle$ and $|AB^*\rangle$. The AIFDEM scheme[70,71] approximates $|A^*B\rangle$ and $|AB^*\rangle$ by direct product states $|\Psi_A^*\Psi_B\rangle$ and $|\Psi_A\Psi_B^*\rangle$, respectively, where $|\Psi_A^*\rangle$ represents the first excited state of the isolated monomer A. $|\Psi_B\rangle$ represents the ground state of fragment B, which is written by a single SCF determinant $|\Phi_B\rangle$. The AIFDEM scheme expresses $|\Psi_A^*\rangle$ as a spin-adapted CSF(configuration state function) by linear combinations of singly-excited determinants:

$$|\Psi_A^*\rangle = \sum_{ia} \sum_{\sigma=\alpha,\beta} C_\sigma^{ia} |\Phi_A^{ia}\rangle, \tag{8}$$

where the ith occupied σ-spin orbital in Φ_A is replaced with the ath virtual σ-spin in Φ_A^{ia}. The non-diagonal element of the excitonic Hamiltonian is, therefore, written by

$$\langle \Psi_A^* \Psi_B | \hat{H} | \Psi_A \Psi_B^* \rangle = \sum_{ia\sigma} \sum_{kb\tau} C_\sigma^{ia} C_\tau^{kb} \langle \Phi_A^{ia} \Phi_B | \hat{H} | \Phi_A \Phi_B^{kb} \rangle. \tag{9}$$

In the AIFDEM scheme, the excitonic basis states are not orthogonal to each other:

$$\langle \Psi_A^* \Psi_B | \Psi_A \Psi_B^* \rangle = \sum_{ia\sigma} \sum_{kb\tau} C_\sigma^{ia} C_\tau^{kb} \langle \Phi_A^{ia} \Phi_B | \Phi_A \Phi_B^{kb} \rangle \neq 0. \tag{10}$$

Therefore, one has to use the Löwdin orthogonalized technique[72] to obtain the excitonic coupling as follows:

$$V = \frac{\langle \Psi_A^* \Psi_B | \hat{H} | \Psi_A \Psi_B^* \rangle - \langle \Psi_A^* \Psi_B | \Psi_A \Psi_B^* \rangle \left(E_{A^*B} + E_{AB^*} \right) / 2}{1 - \langle \Psi_A^* \Psi_B | \Psi_A \Psi_B^* \rangle^2}, \tag{11}$$

where E_{A^*B} and E_{AB^*} represent $\langle \Psi_A^* \Psi_B | \hat{H} | \Psi_A^* \Psi_B \rangle$ and $\langle \Psi_A \Psi_B^* | \hat{H} | \Psi_A \Psi_B^* \rangle$, respectively. Because the direct product states $|\Psi_A^* \Psi_B\rangle$ and $|\Psi_A \Psi_B^*\rangle$ are the excitonic basis states in Eq. 11, the CT states corresponding to A^+B^- (cation-anion pair) and A^-B^+ (anion-cation pair) are not involved in the excitonic coupling calculations.

This study used the AIFDEM scheme implemented in Q-Chem Version 5.1 suite of programs.[73] We performed the CIS (configuration interaction singles) calculations for obtaining the $|\Psi_A^* \Psi_B\rangle$ and $|\Psi_A \Psi_B^*\rangle$ with the 85 % threshold of the norm of monomer natural-transition-orbital (NTO) amplitudes taking into account the single excited determinants in Eq. 8.

FED and ER-D Schemes

Here, we again regard the special-pair model as a system of two chromophores, A and B, and express two (quasi-)diabatic electronic states by $|A^*B\rangle$ and $|AB^*\rangle$. The FED and ER-D schemes are similar to each other. The two methods assume that only local excitations within each monomer are involved in the intra-dimer EET and perform the unitary transformation

of the two-state excitonic Hamiltonian from an adiabatic form to a diabatic one,

$$\begin{pmatrix} E_{A^*B} & V \\ V & E_{AB^*} \end{pmatrix} = \mathbf{U} \begin{pmatrix} E_1 & 0 \\ 0 & E_2 \end{pmatrix} \mathbf{U}^T. \tag{12}$$

E_1 and E_2 in the adiabatic Hamiltonian are the first and second singlet-excited state energies of the dimer, respectively. E_{A^*B} and E_{AB^*} are the (quasi-)diabatic state energies of $|A^*B\rangle$ and $|AB^*\rangle$, respectively. The unitary matrix $\mathbf{U}$ for the FED scheme is determined using the electron attachment and hole detachment densities[74] created in the excitation and the excitionic coupling between the pigment-pair A and B is written as[50]

$$V^{\mathrm{FED}} = \frac{(E_2 - E_1)|\Delta x_{12}|}{\sqrt{(\Delta x_{11} - \Delta x_{22})^2 + 4\Delta x_{12}^2}}, \tag{13}$$

where E_1 and E_2 are S_1- and S_2-state energies of the special pair, in this study. The excitation difference Δx_{ij} in the equation is defined by

$$\begin{aligned} \Delta x_{ij} &= x_{ij}^{(A)} - x_{ij}^{(B)} \\ &= \int_{\mathbf{r}\in(A)} \mathrm{d}\mathbf{r}\rho_{\mathrm{ex}}^{ij}(\mathbf{r}) - \int_{\mathbf{r}\in(B)} \mathrm{d}\mathbf{r}\rho_{\mathrm{ex}}^{ij}(\mathbf{r}), \end{aligned} \tag{14}$$

where $\mathbf{r} \in (A)$ represents the region of the pigment A. $\rho_{\mathrm{ex}}^{ij}(\mathbf{r})$ is the sum of attachment and detachment densities[74] for the transition from the ith adiabatic state of the dimer to the jth adiabatic state as follows:

$$\rho_{\mathrm{ex}}^{ij}(\mathbf{r}) = \rho_{\mathrm{hole}}^{ij}(\mathbf{r}) + \rho_{\mathrm{elec}}^{ij}(\mathbf{r}). \tag{15}$$

On the other hand, Subotnik and coworkers[51,52] have developed a diabatization scheme using the famous Edmiston–Ruedenberg localization technique,[75] called ER-D. Here, we express the first and second singlet-excited states calculated for the special-pair model by $|1\rangle$ and $|2\rangle$, respectively, which are the adiabatic excitonic states. By using the unitary matrix

$\mathbf{U}$, the $|A^*B\rangle$ and $|AB^*\rangle$ are constructed by the linear combinations of $|1\rangle$ and $|2\rangle$,

$$\begin{pmatrix} |A^*B\rangle \\ |AB^*\rangle \end{pmatrix} = \mathbf{U}^T \begin{pmatrix} |1\rangle \\ |2\rangle \end{pmatrix} = \begin{pmatrix} U_{11}|1\rangle + U_{21}|2\rangle \\ U_{12}|1\rangle + U_{22}|2\rangle \end{pmatrix}. \tag{16}$$

The ER-D scheme determines $\mathbf{U}$ by maximizing self-interaction energy,

$$F_{\mathrm{ER}}(\mathbf{U}) = \sum_{I=1}^{2} \int \mathrm{d}\mathbf{R}_1 \int \mathrm{d}\mathbf{R}_2 \frac{\langle I|\hat{\rho}(\mathbf{R}_2)|I\rangle\langle I|\hat{\rho}(\mathbf{R}_1)|I\rangle}{|\mathbf{R}_1 - \mathbf{R}_2|}. \tag{17}$$

When defining the position of jth electron by $\mathbf{r}_j$, the density operator at position $\mathbf{R}$ is expressed as

$$\hat{\rho}(\mathbf{R}) = \sum_j \delta^3(\mathbf{R} - \mathbf{r}_j). \tag{18}$$

In this work, we used the FED and ER-D schemes implemented in the Q-Chem Version 5.1 suite of programs.[73] To obtain the first and second excited states (S_1 and S_2) of the P800 and P700 models used for both the schemes, we performed the CIS (configuration interaction singles) calculations on the P800 and P700 models.

As mentioned above and discussed in detail in Ref. 37, there is a risk that the FED and ER-D schemes fail to estimate the excitonic couplings because of the CT-state contamination in the S_1 and S_2 states calculated for the P800 and P700 models. Therefore, to assess the applicability of the FED and ER-D schemes, we examined the CT natures of the calculated S_1 and S_2 by using the "libwfa" library[76,77] implemented in Q-Chem and the "TheoDORE" program.[53] In these analyses, the CT nature is evaluated by a descriptor called CT character (CT), which is based on the one-electron transition density matrix corresponding to the excitation of interest.[53]

To address the dependence of the calculated CT values on the used methods, in addition to the CIS calculations used for the FED and ER-D schemes, we performed the TD-DFT calculations with a CIS-like Tamm-Dancoff approximation (TDA). This study used the global hybrid B3LYP and BH&HLYP[78,79] and long-range corrected LC-BOP[80,81] and

CAM-B3LYP[65] density functionals for the TD-DFT calculations with TDA. The degrees of HF exchange in the B3LYP and BH&HLYP functionals are 20 % and 50%, respectively. The range-separated parameters of the LC-BOP and CAM-B3LYP functionals are set to 0.33 Bohr^{-1}.

RESULTS

TrESP Charges

Table 1 lists the vertical excitation energy (VEE), oscillator strength (OS), and the amplitude of the TDM ($|\mu|^{\text{Calc.}}$) obtained for the first-excited state of each pigment model in the gas phase by TrESP method. Figure 3(a) plots the corresponding transition densities on models of BChl-*g* and Chl-*a*. The S_1 and S_2 electronic transitions of a (bacterio)chlorophyll are generally named Q_y and Q_x, respectively, and each transition gives a peak in the absorption spectrum.[82,83] The TD-CAM-B3LYP calculations show that both the "HOMO→LUMO (π–π^*)" transition dominantly and "HOMO−1 → LUMO+1 (π–π^*)" transition slightly contribute to their $S_1(Q_y)$ excitations, respectively. This behavior is consistent with the interpretation based on the Gouterman model. (See Refs. 82,83) On the other hand, only the "HOMO−1 → LUMO (π–π^*)" transition dominantly contributes to $S_2(Q_x)$. All the resultant TDMs of S_1 (Q_y) lie nearly along the molecular y-axis connecting the nitrogen atoms of ring I and ring III. The resultant OS's are as large as expected, which verifies their bright Q_y states. The BChl-*g* (Chl-*a*) model yields the results similar to those for the BChl-*g*' (Chl-*a*') as the stereoisomerization at the 13^2 position of ring III has a small impact on the electronic structure of (bacterio)chlorophyll. The TD-CAM-B3LYP calculations always yield a substantial blue-shift in VEEs compared to the experimental values $\text{VEEs}^{\text{Expr.}}$ and yield larger $|\mu|^{\text{Calc.}}$ compared to the $|\mu|^{\text{Expr.}}$. We, therefore, rescaled the TrESP charges obtained from the TD-CAM-B3LYP results by the ratio $|\mu|^{\text{Expr.}}/|\mu|^{\text{Calc.}}$ for the subsequent Poisson-TrESP calculations. Tables S6–S10 in Supporting Information list the rescaled TrESP charges for

the five pigment models. Figure 3(b) plots the rescaled TrESP charges for the BChl-g and Chl-a models. It should be notable that absolute values of scaled TrESP charges at CHC, C4C, and CHD on BChl-g are prominently different from on Chl-a.

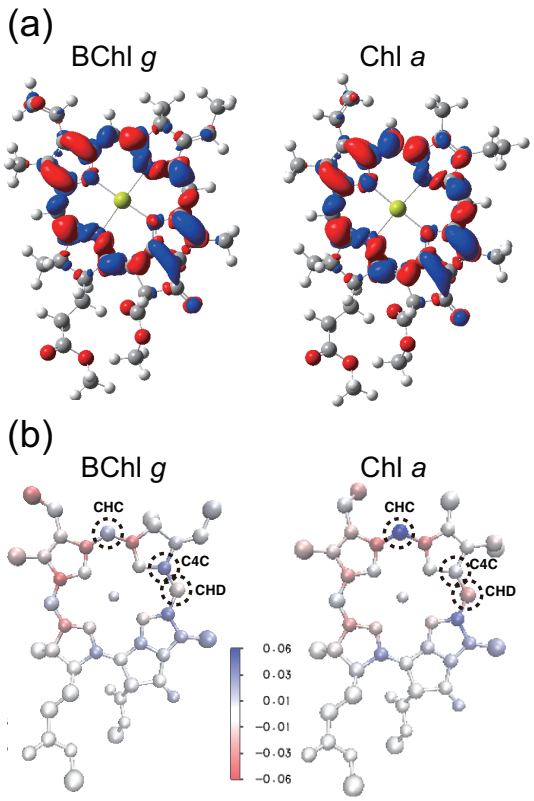

Figure 3: (a) Transition electron densities and (b) scaled TrESP charges of BChl-g and Chl-a pigment models.

Poisson-TrESP Method

We applied the Poisson-TrESP (Eqs. 5 and 7) method for the calculations of the Förster-type Coulomb couplings among all pigments in hRC and PSI. Comparisons of the couplings in hRC between the TrESP method (Eq. 4) and the Poisson-TrESP method with the vacuum case ($\epsilon = 1$) are shown in Figure S1 in Supporting Information. We can see that the $V^{\mathrm{P-TrESP}}(\epsilon = 1)$-values agree well with the V^{TrESP}-values. It indicates that the errors arising from the numerical solutions of the Poisson equation with the finite-difference method are negligible. The obtained $V^{\mathrm{P-TrESP}}(\epsilon = 2)$-values were compared with the $V^{\mathrm{P-TrESP}}(\epsilon = 1)$-

Table 1: Vertical excitation energy, VEE (in eV); oscillator strength, OS; and the amplitude of TDM, $|\mu|^{\text{Calc.}}$ (in Debye) calculated with the TD-CAM-B3LYP/cc-pVDZ method for the five pigment models from hRC and PSI in the gas phase. The corresponding experimental values ($\text{VEE}^{\text{Expr.}}$ and $|\mu|^{\text{Expr.}}$) are also listed. The details of each Chl are stated in the text.

Pigment Model	VEE	OS	$\lvert\mu\rvert^{\text{Calc.}}$	$\text{VEE}^{\text{Expr.}}$	$\lvert\mu\rvert^{\text{Expr.}\,a}$
BChl-g	1.732	0.373	7.524	1.579	6.5
BChl-g'	1.739	0.340	7.166	1.579	6.5
Chl-a_F	2.096	0.213	5.168	1.851	4.6
Chl-a	2.071	0.231	5.421	1.851	4.6
Chl-a'	2.075	0.225	5.341	1.851	4.6

[a] Knox and Spring determined the values from an empty cavity analysis from absorption data of (bacterio)chlorophylls in different solvents.

values in hRC and PSI as shown in Figures 4(a) and (b), respectively. Solid red lines represent the least-squares fitting lines for the relation between $V_{m,n}^{\text{P-TrESP}}(\epsilon = 2)$ and $V_{m,n}^{\text{P-TrESP}}(\epsilon = 1)$ calculated after omitting the intra-special-pair couplings for P800 and P700. The slopes of the fitting lines in Figure 4(a)–(b) are ca. 0.70, which is very close to that of 0.69 reported by Renger and Müh in the PSI trimer complex.[40] It indicates that the mean local field correction/screening factors obtained for hRC and PSI are almost identical.

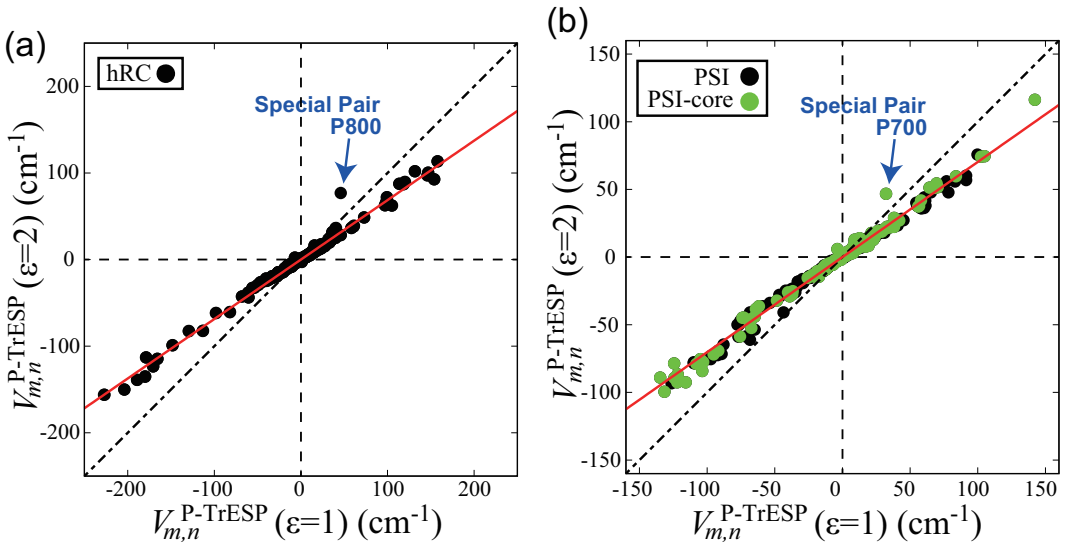

Figure 4: Correlation between Förster-type Coulomb couplings in (a) hRC and (b) PSI obtained by using Eq. 7 with ϵ of 2 and with ϵ of 1 (vacuum). The solid red lines represent the least-squares fitting ones. The closed green circles represent the results for pigment pairs in PSI-core.

Next, we address the evaluation of the individual local-field correction/screening factors $f_{m,n} = V_{m,n}^{\mathrm{P-TrESP}}(\epsilon = 2)/V_{m,n}^{\mathrm{P-TrESP}}(\epsilon = 1)$. The distance dependences of $f_{m,n}$ obtained for hRC and PSI, respectively, are shown in Figures 5(a) and (b), where only the results with $\left|V_{m,n}^{\mathrm{P-TrESP}}(\epsilon = 2)\right| > 5$ cm^{-1} are plotted. Figure 5 indicates no systematic dependence of $f_{m,n}$ on the inter-pigment distance $R_{m,n}$ for hRC as well as for PSI, which is consistent with the previous study[40] for the PSI-trimer complex. The resultant $f_{m,n}$ exceeds a value of 1 only for a few pigment pairs, which is called an off-size screening factor in Ref. 47 and is discussed later in detail.

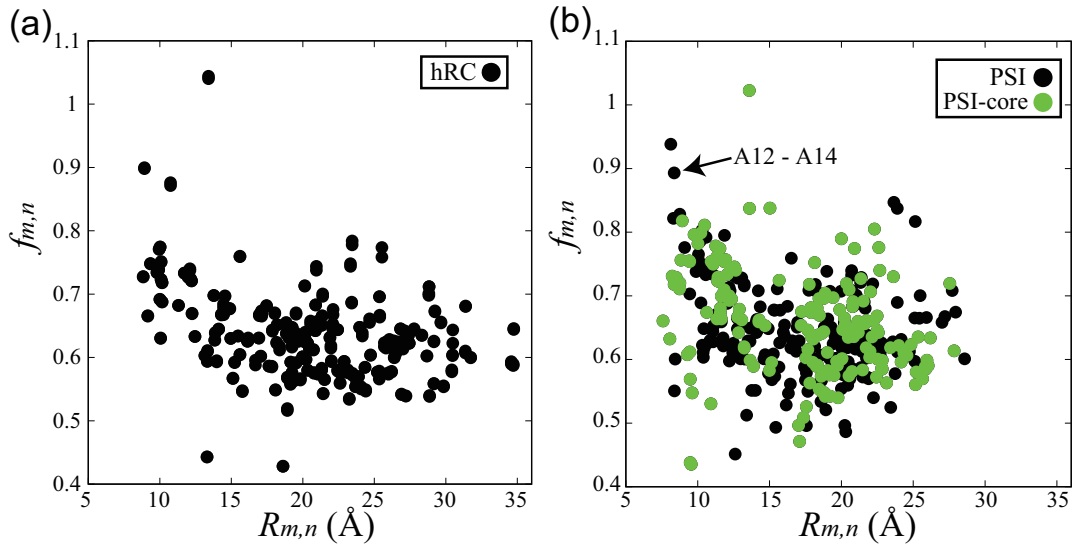

Figure 5: Correlation between Mg-to-Mg distance, $R_{m,n}$ and the local field correction/screening factors $f_{m,n}$ for Förster-type Coulomb couplings in (a) hRC and (b) PSI. Only the results with $\left|V_{m,n}^{\mathrm{P-TrESP}}(\epsilon = 2)\right|$ larger than 5 cm^{-1} are plotted. The closed green circles represent the results for pigment pairs in PSI-core.

Next, the $\left|V_{m,n}^{\mathrm{P-TrESP}}(\epsilon = 2)\right|$-values are compared with the $\left|V_{m,n}^{\mathrm{dd}}\right|$-values in a vacuum ($f = 1$) of Eq. 2 for hRC and PSI in Figure 6(a) and (b), respectively. Figure 6(a) does not include P800 in hRC because the dd-interaction method yields an extraordinarily high value of $1,025$ cm^{-1} for the intra-special-pair coupling of P800, as described in Ref. 17. Figure 6(a) indicates that the simple dd-interaction method can approximate the more accurate $V_{m,n}^{\mathrm{P-TrESP}}(\epsilon = 2)$ at a local field correction/screening factor f^{dd} of 0.56. In contrast, Figure 6(b) shows that the dd-interaction method is invalid for PSI, as reported previously for the PSI-trimer complex

by Adolphs et al..[39] (All data set in hRC and PSI with the TrESP, Poisson-TrESP, and dd-interaction methods are provided in Supporting Information.)

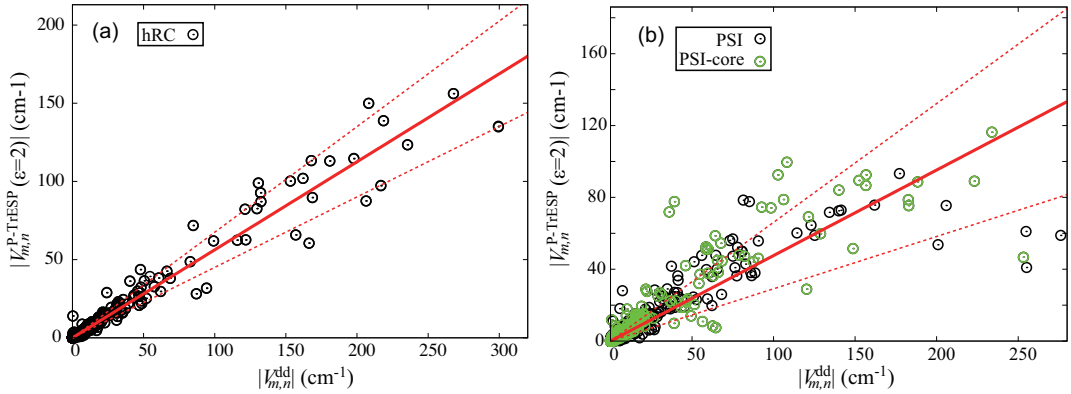

Figure 6: Correlation between the absolute Förster-type Coulomb couplings in (a) hRC and (b) PSI obtained by using Eq. 7 with ϵ_{opt} of 2 and Eq. 2 in vacuum. The solid red lines represent the least-squares fitting lines. The open green circles represent the results for pigment pairs in PSI-core. The dashed red lines represent standard deviation from the fitting line.

Excitonic Couplings of Special Pair

As marked by the blue arrows in Figure 4, the Poisson-TrESP method with $\epsilon = 1$ yields 45.87 cm^{-1} and 32.24 cm^{-1} for the Förster-type Coulomb couplings of P800 and P700, respectively. The coupling values are significantly smaller than the corresponding parameters (138 – 250 cm^{-1}) used in the previous theoretical studies.[17,19,39] Madjet et al.[48] pointed out that the short-range coupling mechanism, including Dexter-type exchange one, dominantly works in the EETs within the special pairs. We here calculated the excitonic couplings of the P800 and P700 models, by taking the short-range coupling mechanism into account.

Table 2 lists the resultant values. The AIFDEM method yields the excitonic couplings of 270.0 cm^{-1} and 206.7 cm^{-1} for the P800 and P700, respectively. The resultant excitonic couplings are significantly larger than the corresponding Coulomb couplings calculated by the Poisson-TrESP method. Therefore, the results from the AIFDEM scheme indicate that the short-range coupling mechanism is effective in the excitonic couplings of P800 and P700.

Table 2: Excitonic couplings of P800 and P700 models calculated with the AIFDEM, FED, and ER-D schemes. The CIS and TD-LC-BOP calculations with the 6-31G(d) basis sets were performed.

Diabatization Scheme	Excited State Calculation	Couplings (cm^{-1})	
		P800	P700
AIFDEM	CIS	270.0	206.7
FED	CIS	234.2	129.8
	TD-LC-BOP	164.1	117.9
ER-D	CIS	234.2	129.8
	TD-LC-BOP	164.1	117.9

Both the FED and ER-D schemes based on the CIS calculations provide the almost identical couplings for each special pair model, as listed in Table 2. The coupling of 129.8 cm^{-1} obtained for P700 is close to 138 cm^{-1} derived from the extended dipole approximation for the Coulomb coupling by Byrdin et al..[19] The coupling of 234.2 cm^{-1} obtained for P800 is also close to 250 cm^{-1} that was used in the theoretical model of our previous paper.[17] In comparison with the results from the Poisson-TrESP method, both the FED and ER-D schemes, therefore, indicate that the short-range coupling mechanism dominantly contributes to the excitonic couplings of P800 and P700.

Through the study on the special pair (BChl-*b* dimer) in the RC of purple bacteria, Hasegawa et al.[82] have shown that one can understand the lower excited states of the special pair on the basis of those of the monomer as follows: each monomer state splits into four, including two locally-excited Frenkel exciton (Ex) and two CT states, by its dimerization. Consequently, the Q_y and Q_x split into the eight states in total, which are significantly involved in the lower excited states of the special pair. (See the details in Figure 5 of Ref. 82.) When constructing the diabatic basis $|A^*B\rangle$ and $|AB^*\rangle$, the AIFDEM scheme accounts for the limited number of (important) single excitations within each isolated monomer (A or B) of the dimer (AB) at the CIS level of theory. Therefore, the AIFDEM scheme provided the S_1 and S_2 of P800 and P700 as the pure Frenkel exciton states consisting of Q_y of each monomer. Hereafter, we call the Frenkel state Ex(Q_y). On the other hand, since the FED and ER-D schemes account for all the single excitations within the dimer, they are more accurate

than the AIFDEM. However, there is a risk that Ex(Q_y) states significantly mix with the CT states in the S_1 and S_2 of dimer, which degrades the excitonic coupling calculations from the FED and ER-D schemes. To check the applicability of the FED and ER-D schemes to the excitonic coupling calculations of the P800 and P700 models, we examined the CT character (CT) of S_1 and S_2 obtained from the CIS calculations. Table 3 lists the VEE, OS, and CT obtained for the P800 and P700 models. We can see that the CIS calculations yield S_1 with large OS for both P800 and P700. On the other hand, S_2 from the CIS calculation has the much smaller OS than that of S_1. These results reflect the fact that the special pair models form roughly "J-aggregate" states. The CT values of S_1 and S_2 from the CIS calculations are close to zero, indicating that the resultant S_1 and S_2 are almost Ex(Q_y) states. Therefore, the CT-state contamination is negligible in the FED and ER-D results based on the CIS calculations. Table 3 also lists the results on S_3 from the CIS calculations. The two-state approximation used in the FED and ER-D schemes are valid because of large energy differences between S_1/S_2 and S_3 states. We can, therefore, apply the FED and ER-D schemes with the CIS results to the excitonic couplings of the P800 and P700 models.

Table 3 also lists the results from the TD-BH&HLYP and TD-LC-BOP calculations. Table S13 in Supporting Information lists the results from the TD-B3LYP and TD-CAM-B3LYP calculations. The TD-DFT calculations with the B3LYP and BH&HLYP functionals, provided the large CT values of S_1 and S_2 for P800. Because the calculated CT values are close to 1, S_1 and S_2 from the TD-B3LYP and TD-BH&HLYP calculations for the P800 model are almost CT excited (or charge resonance) states. These results are related to the famous problem of the TD-DFT with the global hybrid density functionals:[84] *i.e.*, the underestimation of CT state energies. Therefore, the FED and ER-D schemes with the TD-B3LYP and TD-BH&HLYP results are inapplicable to the calculations of excitation coupling of the P800 model. The TD-B3LYP also provided the large CT values for S_1 and S_2 of the P700 model. In contrast, interestingly, the TD-BH&HLYP provided small CT values of 0.134 and 0.038 for S_1 and S_2 of the P700 model, respectively.

Table 3: Vertical excitation energy, VEE (in eV); oscillator strength, OS; and charge-transfer characteristic (CT) calculated with the CIS and TD-DFT with TDA for the P800 and P700 models in the gas phase. The 6-31G(d) basis sets were used.

Model	Method	State	Character[a]	VEE	OS	CT
P800	CIS	S_1	Ex(Q_y)	1.941	0.839	0.0857
		S_2	Ex(Q_y)	1.999	0.147	0.0200
		S_3	Ex(Q_x) + CT	2.477	0.006	0.3584
	TD-LC-BOP	S_1	Ex(Q_y)	1.814	0.682	0.1143
		S_2	Ex(Q_y)	1.854	0.104	0.0399
	TD-BH&HLYP	S_1	CT + Ex(Q_y)	1.762	0.323	0.7316
		S_2	CT	1.802	0.006	0.8681
P700	CIS	S_1	Ex(Q_x)	2.372	0.475	0.0130
		S_2	Ex(Q_y)	2.420	0.148	0.0104
		S_3	Ex(Q_x)	3.382	0.045	0.0739
	TD-LC-BOP	S_1	Ex(Q_y)	2.251	0.330	0.0204
		S_2	Ex(Q_y)	2.289	0.095	0.0137
	TD-BH&HLYP	S_1	Ex(Q_y)	2.314	0.411	0.1340
		S_2	Ex(Q_y)	2.373	0.0796	0.0378

[a] Ex and CT represent Frenkel exciton and charge-transfer states, respectively. Q_y and Q_x in the parentheses represent the monomer state forming the Ex.

We also performed TD-LC-BOP and TD-CAM-B3LYP calculations on the P800 and P700 models. Similar to the CIS calculations, the TD-CAM-B3LYP calculations yielded S_1 with large OS, and with small OS for the P800 model. However, the TD-CAM-B3LYP calculations provided the CT values of 0.533 and 0.585 for S_1 and S_2 of P800, respectively, indicating that the CT excited states are equally mixed with locally excited states in S_1 and S_2. Therefore, the FED and ER-D schemes with the TD-CAM-B3LYP results are inapplicable to the excitation-coupling calculations of the P800 model. In contrast, the TD-LC-BOP provided the small CT values of 0.114 and 0.040 for S_1 and S_2 of the P800 model, which likely supports the application of the FED and ER-D schemes with these S_1 and S_2 results. For S_1 and S_2 of the P700 model, the TD-LC-BOP and TD-CAM-B3LYP calculations always provided the negligibly small CT values, similar to the CIS calculations.

Judging from the CT values, we calculated the excitonic coupling of P800 by using the FED and ER-D schemes with the TD-LC-BOP results. Similarly, we calculated the excitonic

coupling of P700 by using the FED and ER-D schemes with the TD-LC-BOP, TD-CAM-B3LYP, and TD-BH&HLYP results. We list the results from TD-LC-BOP in Table 2. The other results are listed in Table S14 in Supporting Information. Although the results roughly agree with ones from the CIS calculations, we found that the calculated excitonic couplings depend on the employed density functionals to some extent.

DISCUSSION

Numerical Calculation of Excitonic Couplings on hRC

We calculated the excitonic couplings among the BChl-g pigments in the hRC protein on the basis of the X-ray structure by Gisriel et al..[1] Our previous study[17] used the conventional dd-interaction method for the calculations. This study used the more accurate Poisson-TrESP method for the calculations of the Förster-type Coulomb couplings. Only for the special pair, P800, we took into account the short-range excitonic-coupling contributions by using AIFDEM, FED, and ER-D schemes, as discussed later. We also calculated the excitonic couplings among the Chl-a pigments in the PSI protein for the comparison. We found that the mean local field correction/screening factor $f = 0.70$ for both the hRC and PSI by comparing the $V_{m,n}^{\mathrm{P-TrESP}}(\epsilon = 2)$ and $V_{m,n}^{\mathrm{P-TrESP}}(\epsilon = 1)$ (Figure 4). The f value estimated for the PSI-monomer in this study is consistent with those reported by Renger's group[39,40] for monomer and trimer of PSI. We observed no systematic dependence of the individual local-field correction/screening factors $f_{m,n}$ on the corresponding inter-pigment distances $R_{m,n}$ for hRC and PSI, as shown in Figure 5. The distance-independence is consistent with the previous study.[40] We then compared the $V_{m,n}^{\mathrm{P-TrESP}}(\epsilon = 2)$-values with $V_{m,n}^{\mathrm{dd}}$-values for hRC and PSI. We found the breakdown of the dd-interaction approximation for PSI (Figure 6(b)), reconfirming the results by Adolphs et al..[39] On the other hand, we observed that the dd-interaction method approximates the Coulomb couplings available from the Poisson-TrESP method for the hRC pigments (Figure 6(a)). The observation supports our

previous analysis[17] on the EETs in hRC with the dd-interaction method.

The practical procedures of application of the Poisson-TrESP method in this study is a little different from those reported by Renger's group.[39,40] We used the TD-CAM-B3LYP/cc-pVDZ calculations for the TrESP charges, while the TD-B3LYP/6-31G(d) has been used in literature. We used the UA0 parameters for the atomic radii in the numerical Poisson equation, while they used the CHARMM22 force field parameters.[85] These differences may affect the results. For example, Renger and Müh observed $f_{m,n} = 1.06$ for the A12–A14 (or 1112–1114) pair in PSI, which is a strongly coupled J-type dimer located at the periphery of PSI.[54] On the other hand, we observed a little smaller $f_{m,n} = 0.88$ for the pair, as marked by the arrow in Figure 5(b). However, the value is still larger than the mean value at $f = 0.70$. Therefore, we believe that our calculations for PSI reasonably reproduced the results by Renger's group and can be compared with those on hRC to characterize the features of different RCs.

Figure 5 shows off-size screening factors, i.e. $f_{m,n} > 1$, only for a few pigment pairs. We observed $f_{m,n} = 1.04$, $R_{m,n} = 13.4$ Å, $\kappa^2_{m,n} = 0.058$, and $V^{\mathrm{P-TrESP}}_{m,n}(\epsilon = 1) = 15.7$ cm^{-1} for the pigment pairs 8–15 and 38–45 (or 1008 – 1015 in PDB) on hRC. We observed $f_{m,n} = 1.02$, $R_{m,n} = 13.6$ Å, $\kappa^2_{m,n} = 0.0044$, and $V^{\mathrm{P-TrESP}}_{m,n}(\epsilon = 1) = 8.33$ cm^{-1} for the pigment pair 1216 – 1220 on PSI. As explained in Ref. 47, off-size screening factors appear when $V^{\mathrm{P-TrESP}}_{m,n}$ becomes small excitonic couplings owing to the formation of specific mutual conformations of the pigment pair m-n in the supramolecular complex $\mathbf{P}_{16}$. Similarly, the pigment pairs with off-size screening factors in Figure 5 have the specific small $\kappa^2_{m,n}$, whereas they provide not-so-small $V^{\mathrm{P-TrESP}}_{m,n}$-values.

Excitonic Couplings of Special Pairs

The special pair of RC usually works as a sink for the transferred excitation energy because its site energy is considerably red-shifted by the excitonic coupling of the special pair.[48] The Poisson-TrESP method yielded small couplings of 45.87 cm^{-1} and 32.24 cm^{-1} for P800 in

hRC and P700 in PSI, respectively, which is insufficient to cause the expected large red-shifts by the excitonic coupling. The underestimations are probably due to the lack of the short-range coupling contributions in the Poisson-TrESP calculations. Therefore, we applied the more advanced FED and ER-D schemes with the CIS calculations only to the special pairs and as a result, obtained the couplings of 234.2 cm^{-1} and 129.8 cm^{-1} for P800 and P700, respectively. The resultant values are close to the corresponding parameter values used in the previous theoretical studies[17,19,39] on hRC[17] and PSI.[30] As shown in Ref. 48, it is not only the excitonic coupling that creates the excitation energy sink at the special pair, but also the electron exchange between pigments, which effectively shifts site energy and contributes to the short-range excitonic couplings. We need to numerically analyze both effects to determine the energy sink at the special pairs in hRC and PSI for the future work.

We checked the contamination of the CT states into S_1 and S_2 involved in the coupling calculations of the special pairs because the contamination would disturb the FED and ER-D schemes. Consequently, we obtained the small CT characters at $CT \approx 0$ to S_1 and S_2 from the CIS results with the TheoDORE program.[53] It validates the applicability of the FED and ER-D schemes to the calculations of excitonic coupling of the P800 and P700 models at the CIS level.

Adolphs et al.[39] used the value of 230 cm^{-1} for their analysis of the EET dynamics in PSI. Madjet et al.[48] estimated the excitonic coupling of P700 as ca. 230 cm^{-1} with the TD-BH&HLYP calculations and found that its 80 % arises from the short-range coupling mechanism by using the method based on an effective two-state model that is closely related to the FED scheme,[50] which is also based on the two-state model (Eq. 12) for a pigment dimer, as pointed by Kenny and Kassal.[37] By performing systematic benchmarking calculations of excitonic couplings between BChl molecules, Kenny and Kassal[37] also pointed out that the FED scheme fails to calculate intra-special-pair couplings because the higher-energy transitions involving the CT states would contaminate the calculations and the effective two-state approximation breaks down in those cases.

As discussed above, the excitonic couplings (234.2 cm^{-1} for P800 and 129.8 cm^{-1} for P700) obtained from the FED scheme with the CIS calculations are close to the corresponding parameter values presented in the previous papers.[17,19,39] The FED scheme is valid for the excitonic coupling calculations of the P800 and P700 models in this study, because the CT characters of S_1 and S_2 from the CIS calculations with the TheoDORE program[53] are close to 0, as listed in Table 3. In the AIFDEM scheme, the CT states are not involved in the excitonic coupling calculations because the two (quasi-)diabatic states, $|\Psi_A^* \Psi_B\rangle$ and $|\Psi_A \Psi_B^*\rangle$, are constructed from only single excitations within each monomer of dimer (Eq. 8). The AIFDEM scheme roughly reproduced the results by the FED and ER-D schemes, which also supports the applicability of the FED and ER-D schemes with the CIS calculations to the special-pair-couplings. Hence, the AIFDEM scheme for the excitonic coupling analysis of special pair in hRC/PSI gives less accurate results than FED and ER-D.

We also applied the FED scheme to the TD-DFT results of S_1 and S_2 with $CT \approx 0$, as listed in Table S14 in Supporting Information. The FED scheme with the TD-BH&HLYP result yielded excitonic coupling of 227.4 cm^{-1} for the P700 model, which is close to the result (ca. 230 cm^{-1}) by Madjet et al.[48] based on the same BH&HLYP functional. We observed some dependencies of the excitonic couplings on the employed density functionals.

We should use the results from more advanced correlated *ab initio* QC calculations to assess the performance of the density functionals for the special pair calculations within the framework of TD-DFT, such as the ADC(2) (algebraic-diagrammatic construction through second order) and CC2 (approximated second-order coupled cluster), as the references.[86] Such studies are left for the future work.

Relationship between the Arrangements of BChl-g on hRC and Chl-a on PSI

In this study, we confirmed the applicability of the dd-interaction approximation to the Förster-type Coulomb couplings in hRC. Therefore, we address the question whether the

applicability comes from the pigment arrangement or the (electronic-structure) properties of BChl-g molecule itself on hRC. Previous studies reported that the validity of the dd-interaction approximation depends on the considered photosynthetic systems.[38,41,43,45,87]

Hereafter, let us define "PSI-core" as the group of 57 Chl-a selected in PSI shown by solid blue sticks in Figure 1(e). The pigment arrangement on the hRC resembles that on the PSI-core as seen in the superposition of the arrangement of BChl-g on hRC with that of Chl-a on PSI in Figure 1(e). We used the "align" command of PyMOL software[88] that best aligns the C_α positions in hRC and PSI. We selected 57 out of 96 Chl-a in PSI that are located close to 60 pigments (54 BChl-g, 4 BChl-g', and 2 Chl-a_F) on hRC by using the criterion

$$\min \left[\left| \mathbf{r}_{\mathrm{hRC}}^{(m)} - \mathbf{r}_{\mathrm{PSI}}^{(n)} \right| \right], \tag{19}$$

where $\mathbf{r}_{\mathrm{hRC}}^{(m)}$ ($\mathbf{r}_{\mathrm{PSI}}^{(n)}$) is the coordinate of Mg atom of mth (nth) pigment in hRC (PSI) although we could not obtain the perfect one-to-one matching. The list of the correspondence is given in Table S15 of Supporting Information. In Figure 4(b), the closed green circles represent the correlation between excitonic couplings for PSI-core, as plotted similar to those for hRC in Figure 4(a). It is concluded that mean local field correction/screening factors for hRC BChl-g and PSI-core Chl-a are almost identical. Figure 5(b) indicates no systematic dependence of $f_{m,n}$ on the inter-pigment distance $R_{m,n}$ for PSI-core. It is clearly shown that the dd-interaction method breaks down for PSI-core, as plotted by the open green circles in Figure 6(b) even though the arrangements of pigment pairs in PSI-core resemble those in hRC (see Figure 1(e)).

We, next, address the structural and functional similarities of the two pigment arrangements in more details. Figure 7 plots the correlations of Mg-to-Mg distances $R_{m,n}$, orientation factors $\kappa_{m,n}^2$, and $V_{m,n}^{\mathrm{P-TrESP}}(\epsilon = 2)$ between pigment pairs in hRC and Chl-a pairs in PSI-core. Because of the use of the criterion with Eq. 19, we observed that there is a roughly linear correlation between the $R_{m,n}$'s of pigment on hRC and of Chl-a on PSI-core (Figure 7(a)). There is a weak correlation between the mutual orientation of the pigment pairs in

hRC and PSI-core (Figure 7(b)), when we choose the pairs based from the $R_{m,n}$ values in less than 1 Å (red circles in Figure 7(a)). From the $\kappa^2_{m,n}$-distributions, we conclude that there is a distinct difference in the pigment arrangements between hRC and PSI, though they apparently occupy similar positions, as plotted in Figure 1(e). Figure 7(c) plots the correlation between the resultant $V^{\mathrm{P-TrESP}}_{m,n}(\epsilon = 2)$ values in hRC and PSI-core. We can see that some pigment pairs on hRC and PSI share a reasonable correlation each other, as shown by the red circles in Figure 7(c). The solid red line is the fitted line of the well correlated points with a slope of 0.56. However, we can also see that the correlation of other pairs is weak. These results suggest that the hRC is a system different from the PSI as for the excitonic coupling mechanism.

It is noted that the absolute values of TrESP charges of CHC, C4C, and CHD in BChl-g in Figure 3, are prominently different from those in Chl-a. We, therefore, examined the effects of the electronic properties of pigment molecules on the applicability of the dd-interaction approximation. We recalculated the $V^{\mathrm{dd}}_{m,n}$ and $V^{\mathrm{P-TrESP}}_{m,n}(\epsilon = 2)$ with the TDMs and TrESP charges of Chl-a instead of those of BChl-g. It was easy to replace the TrESP charges of BChl-g with those of Chl-a because BChl-g is an isomer of Chl-a with variation in location of the double bonds. Similarly, the TrESP charges of BChl-g' were replaced with those of Chl-a'. The $|\mu_{m,n}|$-values of BChl-g and BChl-g' were set to 4.6 Debye for the dd-interaction calculations. Figure 8(a) plots the correlation between the resultant $V^{\mathrm{dd}}_{m,n}$- and $V^{\mathrm{P-TrESP}}_{m,n}(\epsilon = 2)$-values. We found that the dd-interaction approximation becomes invalid for the hRC if the TrESP charges of BChl-g are replaced by those for Chl-a. The bold red line in Figure 8(a) shows the fitted line with a slope of $f^{\mathrm{dd}} = 0.57$. The deviation of the calculated couplings from the fitted line in Figure 8(a) is larger than those in Figure 6(a). This result indicates that the differences between the TrESP charges of BChl-g and Chl-a seem to affect the validity of the dd-interaction approximation in hRC. In addition, we recalculated the $V^{\mathrm{dd}}_{m,n}$ and $V^{\mathrm{P-TrESP}}_{m,n}(\epsilon = 2)$ in PSI by replacing the TDMs and TrESP charges of Chl-a with those of BChl-g, and plotted the results in Figure 8(b). The dd-interaction approximation seems

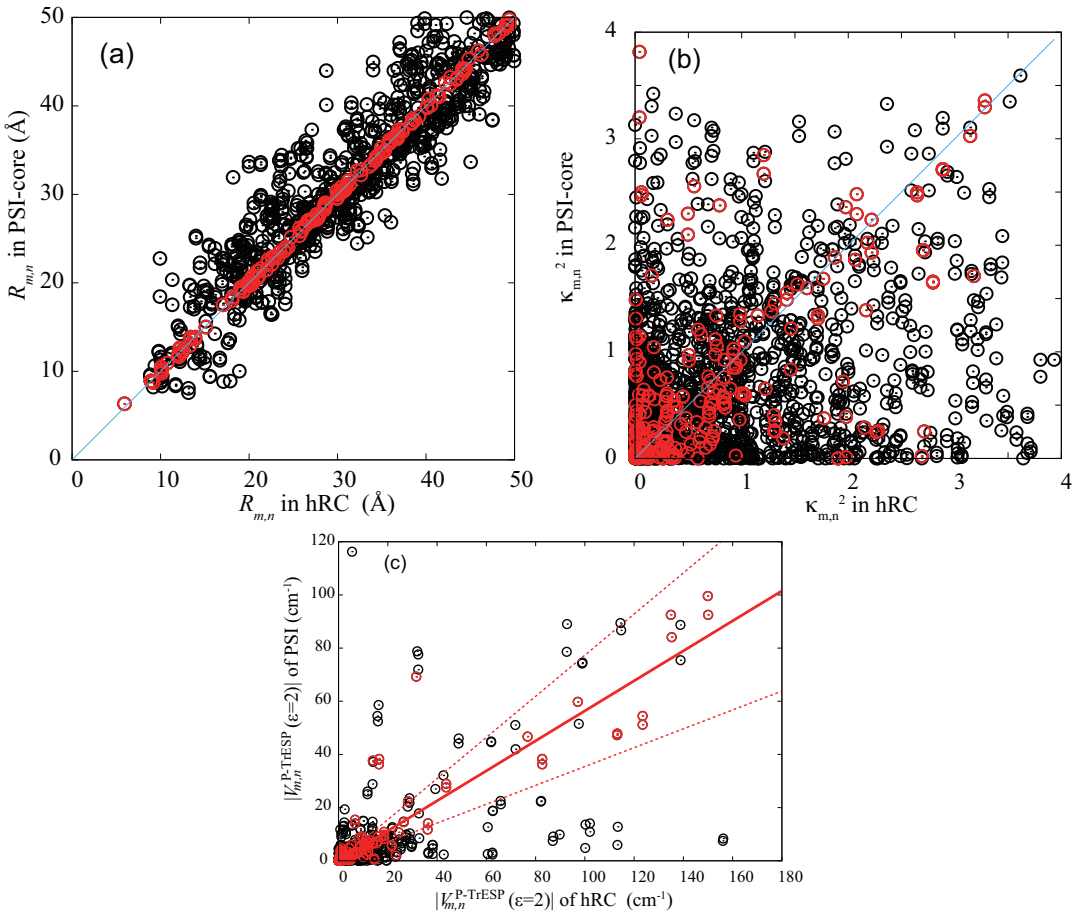

Figure 7: Correlations of (a) Mg-to-Mg distances $R_{m,n}$ (b) orientation factors $\kappa^2_{m,n}$, and (c) $V^{\text{P}-\text{TrESP}}_{m,n}(\epsilon = 2)$ between the hRC and PSI-core pigment-pairs. Only the results with the threshold of $|R^{(\text{hRC})}_{m,n} - R^{(\text{PSI}-\text{core})}_{m,n}| < 1$ Å are plotted with red circle. The dashed red lines represent standard deviation from the fitting line.

to be still breakdown in the PSI, though it depends on the type of the chlorophyll species. From Figures 7 and 8, we can conclude that the conventional dd-interaction approximation becomes valid for the hRC under some conditions, which depend on the specific arrangement of BChl-g, $\kappa^2_{m,n}$-distribution, and the (electronic-structure) properties of pigment molecule itself, etc., that are different from those of Chl-a.

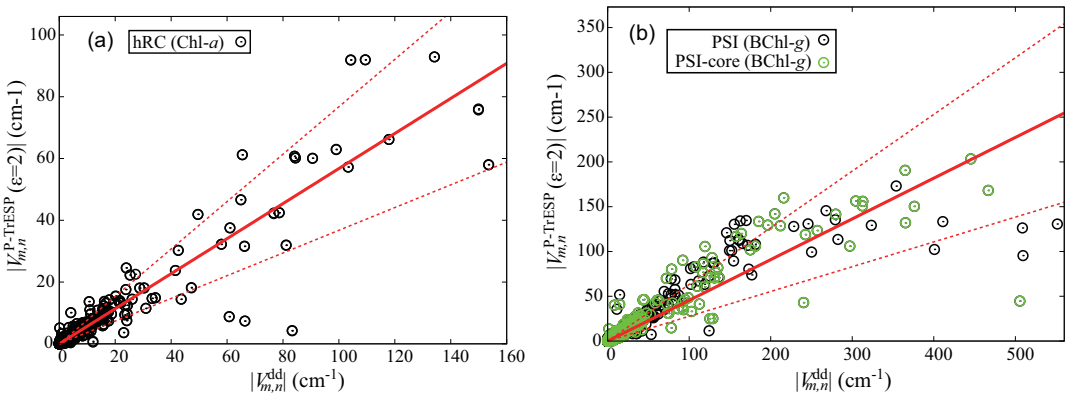

Figure 8: (a) Correlations between the calculated $V^{\rm dd}_{m,n}$ with $|\mu_{m,n}| = 4.6$ Debye and $V^{\rm P-TrESP}_{m,n}(\epsilon = 2)$ with the TrESP charges of Chl-a instead of those of BChl-g in hRC. (b) Correlations between the calculated $V^{\rm dd}_{m,n}$ with $|\mu_{m,n}| = 6.5$ Debye and $V^{\rm P-TrESP}_{m,n}(\epsilon = 2)$ with the TrESP charges of BChl-g instead of those of Chl-a in PSI. The dashed red lines represent standard deviation from the fitting line.

After the replacements of BChl-g by Chl-a on hRC the excitonic coupling strengths become slightly lower (Figure 8(a)). On the other hand, replacements of Chl-a by BChl-g on PSI-core make the excitonic coupling strength a little stronger and improve the reproducibility of the approximation by the excitonic coupling strength of PSI after pigment replacement to BChl-g was a little better in the reproducibility of the approximation by dd calculation (Figure 8(b)). Therefore, by using the quadrupole-quadrupole approximation method, it may be possible to conduct a virtual experiment by pigment we can efficiently estimate the effects of pigment replacement on the excitonic coupling strength. This is the subject of future studies.

Optical Spectra

As shown in Figure 6(a), the Poisson-TrESP results obtained for the hRC protein indicate that the dielectric protein and solvent around the antenna pigments decrease the $V_{m,n}^{\mathrm{dd}}$-values from those in vacuum by about 43 % on average because of the use of optical-dielectric constant value of 2 in the protein environment. Previous study[17] used the vacuum excitonic couplings obtained from the dd-interaction method, which led to the band broadening in the calculated absorption spectrum. On the other hand, the assumption of constant site energy for most of BChl-g on hRC caused the band narrowing. The two types of errors canceled each other, and reproduced the absorption spectrum of hRC rather well.[17] In Figure 2, we plot the absorption spectra of hRC obtained by using the $V_{m,n}^{\mathrm{P-TrESP}}(\epsilon = 2)$ couplings. Exciton states are calculated by simple model (dd excitonic coupling)[17] and by the modified model that replaced dd couplings to Poisson-TrESP couplings with constant site energies. The exciton strengths were weighted by Gaussian distribution with a half width at half maximum of 120 cm^{-1}. We can see that the absorption spectrum calculated with $V_{m,n}^{\mathrm{P-TrESP}}(\epsilon = 2)$ deviates from the experimental one owing to the lack of the (static) disorder of the site energies. More reliable reproduction, therefore, will be realized in the following papers with refined site energy parameters in hRC as done in PSI.[39]

By combining the findings of pigment replacement on PSI/hRC in this study, it might be possible to predict pigment arrangements on gRC that resembles hRC/PSI in many aspects, and functional correlations among the evolutionary related gRC, hRC and PSI.

Yin et al.[49] determined the all excitonic couplings and site energies for Chl-a pigments on PSI by using the CAM-B3LYP method with the quantum-mechanically optimized structure for the entire PSI. As a result, they succeeded in reproducing the Q_y absorption and linear dichroism (LD) spectra for PSI. Yin et al.[49] reported that the X-ray crystal structure provides a poor description of the optical properties. This is probably due to the incorrect coordinate distortions often observed in it. On the other hand, Adolphs et al.[39] also succeeded in reproducing the spectra for PSI by using the Poisson-TrESP method for excitonic couplings

and the charge density coupling (CDC) method[39] for site energies with the X-ray crystal structure. The Poisson-TrESP and CDC methods based on the electrostatic calculations at the molecular force-field level are suitable to apply the X-ray crystal structure because they are not sensitive to the coordinate distortions in it. In this study, we have chosen the Poisson-TrESP for the direct application to the X-ray structure of hRC. More accurate analyses on the spectral properties of hRC would require the methods presented by Yin et al..[49] On the other hand, the Poisson-TrESP and CDC methods provide an adequate balance between accuracy and computational costs for the purpose. Their advantages become more apparent when one uses them in combination with a number of snapshots produced by the molecular dynamics simulations.[36,46,47,89]

This study assumes that the Q_y absorption band of hRC consists of only locally-excited Q_y of its (bacterio)chlorophyll pigments. On the other hand, the ignored CT states might mix with the Q_y band and as a result, modulate the absorption spectrum and light-harvesting efficiency of hRC, as pointed by Cupellini et al.[90] for the LH2 in purple bacteria. In contrast to the dd, Poisson-TrESP, and AIFDEM methods, the effective two-state calculations,[48–52] including FED and ER-D, can empirically take into account those effects through a small amount of the CT contamination. (Madjet et al.[48] studied the effects of the CT states via a super-exchange mechanism.) In this case, one would preferably desire the CT contamination when constructing the simple Frenkel exciton model only from Q_y to study the optical properties. However, when the CT contamination is not small, one needs to construct the Frenkel exciton model explicitly including CT states by using the advanced methods presented by Refs. 90,91. Studies on such cases may be required in the future work.

CONCLUSIONS

We theoretically studied the excitonic couplings among the pigments in the hRC protein on the basis of its 2.2 Å resolution X-ray structure by Gisriel et al..[1] We first calculated the

Förster-type Coulomb couplings by using the more accurate Poisson-TrESP method instead of the standard dd-interaction method employed in our previous study.[17] We also calculated the excitonic couplings among the pigments in the PSI protein for the comparison with those of hRC because PSI is classified into a Type-I RC too and has the pigment arrangement analogous to hRC in its core moiety, as shown in Figure 1(e). We found that the simple dd-interaction approximation is valid for the pigments in hRC, as shown in Figure 6(a). In contrast, Figure 6(b) shows the breakdown of the dd-interaction approximation in PSI, as reported for PSI-monomer and PSI-trimer.[39]

We examined the origin of the differences in the excitonic-coupling features between hRC and PSI via the following procedures. We selected the PSI-core pigments from the PSI-monomer, which almost overlap with the pigment arrangement in the hRC. We identified the differences in the mutual orientation factor $\kappa^2_{m,n}$ and excitonic couplings $V^{\mathrm{P-TrESP}}_{m,n}$ between the pigments on hRC and on PSI-core, as shown in Figure 7. We clarified the effects of the excitonic-couplings by the different transition-density/charges in each pigment of hRC and PSI by the virtual pigment replacement, as shown in Figure 8. From these results, we conclude that the dd-interaction approximation is valid for the hRC pigments because of two major factors: (1) their arrangement in hRC represented by the $\kappa^2_{m,n}$-distribution and (2) the transition density/charges of the BChl-g pigment itself.

The Poisson-TrESP method seems to provide accurate excitonic couplings in some spatially separated pigment pairs in the photosynthetic antenna, but significantly underestimates the excitonic couplings of special pairs, namely, P800 in hRC and P700 in PSI. Therefore, we applied the more advanced FED and ER-D schemes only to the excitonic coupling calculations of P800 and P700, where the short-range coupling mechanism ignored by the Poisson-TrESP method was considered. The resultant coupling values (234.2 cm^{-1} for P800 and 129.8 cm^{-1} for P700) are in good agreement with the corresponding parameter values used for reproducing the spectroscopic data in the previous theoretical studies.[17,19,39] As listed in Table 3, S_1 and S_2 calculated for the P800 and P700 models at the CIS level of the-

ory exhibit the small CT character ($CT \approx 0$), which supports the applicability of the FED and ER-D schemes to their excitonic coupling calculations in the two-state approximation. In addition, we need to investigate all pigment pairs with close inter-molecular distances in hRC with a more accurate method that includes short-range effects, in order to check the accuracies of excitonic couplings by Poisson-TrESP method for the future.

This study confirmed the validation of the dd-interaction approximation, which supports the conclusion of our previous analysis[17] on the EET dynamics in hRC. This study also characterized the unique pigment arrangement of hRC that yields different exciton-coupling states from those of PSI-core, although it apparently resembles that of PSI-core. The unique feature of hRC may reflect the evolutional relation of homodimeric hRC to heterodimeric PSI. PSI seems to have acquired features in the arrangements of pigments and cofactors more complex than those of hRC through the adaptation to the aerobic environment. We will identify the roles of homodimeric (symmetrical) structure of hRC in the EET and charge-separation activities in future works.

Acknowledgement

H. K.-N. acknowledges support from JST, PRESTO Grant Number JPMJPR17G4. S.I. acknowledges support by a grant from KAKENHI (Grant Number 17K07440). The computation in this work has been partly done using the supercomputer of ACCMS, Kyoto University.

Supporting Information Available

Supplementary figures, tables, and text; optimized geometries of pigment, P800, and P700; scaled TrESP charges $\{q_I^{(\mathrm{m})}\}$ and wdWR_I for each pigment model. Data set of the resultant excitonic couplings.

References

(1) Gisriel, C.; Sarrou, I.; Ferlez, B.; Golbeck, J. H.; Redding, K. E.; Fromme, R. Structure of a Symmetric Photosynthetic Reaction Center–Photosystem. *Science* **2017**, *357*, 1021–1025.

(2) Kondo, T.; Matsuoka, M.; Azai, C.; Kobayashi, M.; Itoh, S.; Oh-oka, H. Light-Induced Electron Spin-Polarized (ESP) EPR Signal of the P800+ Menaquinone– Radical Pair State in Oriented Membranes of Heliobacterium modesticaldum: Role/Location of Menaquinone in the Homodimeric Type I Reaction Center. *J. Phys. Chem. B* **2018**, *122*, 2536–2543.

(3) Heinnickel, M.; Golbeck, J. H. Heliobacterial Photosynthesis. *Photosynth. Res.* **2007**, *92*, 35–53.

(4) Rémigy, H.-W.; Stahlberg, H.; Fotiadis, D.; Müller, S. A.; Wolpensinger, B.; Engel, A.; Hauska, G.; Tsiotis, G. The Reaction Center Complex from the Green Sulfur Bacterium Chlorobium tepidum: a Structural Analysis by Scanning Transmission Electron Microscopy. *J. Mol. Biol.* **1999**, *290*, 851 – 858.

(5) Garcia Costas, A. M.; Liu, Z.; Tomsho, L. P.; Schuster, S. C.; Ward, D. M.; Bryant, D. A. Complete Genome of Candidatus Chloracidobacterium thermophilum, a Chlorophyll-Based Photoheterotroph Belonging to the Phylum Acidobacteria. *Environ. Microbiol.* **2012**, *14*, 177–190.

(6) Oh-oka, H. Type 1 Reaction Center of Photosynthetic Heliobacteria †. *Photochem. Photobiol.* **2007**, *83*, 177–186.

(7) Orf, G. S.; Gisriel, C.; Redding, K. E. Evolution of Photosynthetic Reaction Centers: Insights from the Structure of the Heliobacterial Reaction Center. *Photosynth. Res.* **2018**, *138*, 11–37.

(8) Trost, J. T.; Blankenship, R. E. Isolation of a Photoactive Photosynthetic Reaction Center-Core Antenna Complex from Heliobacillus mobilis. *Biochemistry* **1989**, *28*, 9898–9904.

(9) Neerken, S.; Aartsma, T. J.; Amesz, J. Pathways of Energy Transformation in Antenna Reaction Center Complexes of Heliobacillus mobilis. *Biochemistry* **2000**, *39*, 3297–3303.

(10) Liebl, U.; Lambry, J.-C.; Leibl, W.; Breton, J.; Martin, J.-L.; Vos, M. H. Energy and Electron Transfer upon Selective Femtosecond Excitation of Pigments in Membranes of Heliobacillus mobilis. *Biochemistry* **1996**, *35*, 9925–9934.

(11) Nuijs, A. M.; Dorssen, R. J. v.; Duysens, L. N. M.; Amesz, J. Excited States and Primary Photochemical Reactions in the Photosynthetic Bacterium Heliobacterium chlorum. *Proc. Natl. Acad. Sci. U.S.A.* **1985**, *82*, 6865–6868.

(12) Van Noort, P. I.; Gormin, D. A.; Aartsma, T. J.; Amesz, J. Energy Transfer and Primary Charge Separation in Heliobacterium chlorum Studied by Picosecond Time-Resolved Transient Absorption Spectroscopy. *Biochim. Biophys. Acta, Bioenerg.* **1992**, *1140*, 15 – 21.

(13) Lin, S.; Chiou, H.; Kleinherenbrink, F.; Blankenship, R. Time-Resolved Spectroscopy of Energy and Electron Transfer Processes in the Photosynthetic Bacterium Heliobacillus mobilis. *Biophys. J.* **1994**, *66*, 437 – 445.

(14) Miyamoto, R.; Iwaki, M.; Mino, H.; Harada, J.; Itoh, S.; Oh-oka, H. ESR Signal of the Iron-Sulfur Center FX and Its Function in the Homodimeric Reaction Center of Heliobacterium modesticaldum,. *Biochemistry* **2006**, *45*, 6306–6316.

(15) Kondo, T.; Itoh, S.; Matsuoka, M.; Azai, C.; Oh-oka, H. Menaquinone as the Secondary Electron Acceptor in the Type I Homodimeric Photosynthetic Reaction Center of Heliobacterium modesticaldum. *J. Phys. Chem. B* **2015**, *119*, 8480–8489.

(16) Kondo, T.; Matsuoka, M.; Azai, C.; Itoh, S.; Oh-oka, H. Orientations of Iron–Sulfur Clusters FA and FB in the Homodimeric Type-I Photosynthetic Reaction Center of Heliobacterium modesticaldum. *J. Phys. Chem. B* **2016**, *120*, 4204–4212.

(17) Kimura, A.; Itoh, S. Theoretical Model of Exciton States and Ultrafast Energy Transfer in Heliobacterial Type I Homodimeric Reaction Center. *J. Phys. Chem. B* **2018**, *122*, 11852–11859.

(18) Förster, T. In *Modern Quantum Chemistry*; Sinanoglu, O., Ed.; Academic Press: New York, 1965; Vol. III; pp 93–137.

(19) Byrdin, M.; Jordan, P.; Krauss, N.; Fromme, P.; Stehlik, D.; Schlodder, E. Light Harvesting in Photosystem I: Modeling Based on the 2.5-Å Structure of Photosystem I from Synechococcus elongatus. *Biophys. J.* **2002**, *83*, 433 – 457.

(20) Khan, Y. R.; Dykstra, T. E.; Scholes, G. D. Exploring the Förster Limit in a Small FRET Pair. *Chem. Phys. Lett.* **2008**, *461*, 305 – 309.

(21) Muñoz-Losa, A.; Curutchet, C.; Krueger, B. P.; Hartsell, L. R.; Mennucci, B. Fretting about FRET: Failure of the Ideal Dipole Approximation. *Biophys. J.* **2009**, *96*, 4779 – 4788.

(22) Pearlstein, R. M. In *Chlorophylls*; Scheer, H., Ed.; CRC Press, Boca Raton, 1965; pp 1047–1078.

(23) Weiss, C. The Pi Electron Structure and Absorption Spectra of Chlorophylls in Solution. *J. Mol. Spectrosc.* **1972**, *44*, 37 – 80.

(24) Chang, J. C. Monopole Effects on Electronic Excitation Interactions between Large Molecules. I. Application to Energy Transfer in Chlorophylls. *J. Chem. Phys.* **1977**, *67*, 3901–3909.

(25) Sauer, K.; Cogdell, R. J.; Prince, S. M.; Freer, A.; Isaacs, N. W.; Scheer, H. Structure-Based Calculations of the Optical Spectra of the LH2 Bacteriochlorophyll-Protein Complex from Rhodopseudomonas acidophila. *Photochem. Photobiol.* **1996**, *64*, 564–576.

(26) Krueger, B. P.; Scholes, G. D.; Fleming, G. R. Calculation of Couplings and Energy-Transfer Pathways between the Pigments of LH2 by the ab Initio Transition Density Cube Method. *J. Phys. Chem. B* **1998**, *102*, 5378–5386.

(27) Hsu, C.-P.; Fleming, G. R.; Head-Gordon, M.; Head-Gordon, T. Excitation Energy Transfer in Condensed Media. *J. Chem. Phys.* **2001**, *114*, 3065–3072.

(28) Curutchet, C.; Mennucci, B. Toward a Molecular Scale Interpretation of Excitation Energy Transfer in Solvated Bichromophoric Systems. *J. Am. Chem. Soc.* **2005**, *127*, 16733–16744.

(29) Russo, V.; Curutchet, C.; Mennucci, B. Towards a Molecular Scale Interpretation of Excitation Energy Transfer in Solvated Bichromophoric Systems. II. The Through-Bond Contribution. *J. Phys. Chem. B* **2007**, *111*, 853–863.

(30) Scholes, G. D.; Curutchet, C.; Mennucci, B.; Cammi, R.; Tomasi, J. How Solvent Controls Electronic Energy Transfer and Light Harvesting. *J. Phys. Chem. B* **2007**, *111*, 6978–6982.

(31) Curutchet, C.; Scholes, G. D.; Mennucci, B.; Cammi, R. How Solvent Controls Electronic Energy Transfer and Light Harvesting: Toward a Quantum-Mechanical Description of Reaction Field and Screening Effects. *J. Phys. Chem. B* **2007**, *111*, 13253–13265.

(32) Madjet, M. E.; Abdurahman, A.; Renger, T. Intermolecular Coulomb Couplings from Ab Initio Electrostatic Potentials: Application to Optical Transitions of Strongly Coupled Pigments in Photosynthetic Antennae and Reaction Centers. *J. Phys. Chem. B* **2006**, *110*, 17268–17281.

(33) Fujimoto, K. J.; Hayashi, S. Electronic Coulombic Coupling of Excitation-Energy Transfer in Xanthorhodopsin. *J. Am. Chem. Soc.* **2009**, *131*, 14152–14153.

(34) Fujimoto, K. J. Electronic Coupling Calculations with Transition Charges, Dipoles, and Quadrupoles Derived from Electrostatic Potential Fitting. *J. Chem. Phys.* **2014**, *141*, 214105.

(35) Błasiak, B.; Maj, M.; Cho, M.; Góra, R. W. Distributed Multipolar Expansion Approach to Calculation of Excitation Energy Transfer Couplings. *J. Chem. Theory Comput.* **2015**, *11*, 3259–3266.

(36) Maity, S.; Gelessus, A.; Daskalakis, V.; Kleinekathöfer, U. On a Chlorophyll-Caroteinoid Coupling in LHCII. *Chem. Phys.* **2019**, *526*, 110439.

(37) Kenny, E. P.; Kassal, I. Benchmarking Calculations of Excitonic Couplings between Bacteriochlorophylls. *J. Phys. Chem. B* **2016**, *120*, 25–32.

(38) Adolphs, J.; Renger, T. How Proteins Trigger Excitation Energy Transfer in the FMO Complex of Green Sulfur Bacteria. *Biophys. J.* **2006**, *91*, 2778 – 2797.

(39) Adolphs, J.; Müh, F.; Madjet, M. E.-A.; Busch, M. S. a.; Renger, T. Structure-Based Calculations of Optical Spectra of Photosystem I Suggest an Asymmetric Light-Harvesting Process. *J. Am. Chem. Soc.* **2010**, *132*, 3331–3343.

(40) Renger, T.; Müh, F. Theory of Excitonic Couplings in Dielectric Media. *Photosynth. Res.* **2012**, *111*, 47–52.

(41) Müh, F.; Madjet, M. E.-A.; Renger, T. Structure-Based Identification of Energy Sinks in Plant Light-Harvesting Complex II. *J. Phys. Chem. B* **2010**, *114*, 13517–13535.

(42) Müh, F.; Renger, T. Refined Structure-Based Simulation of Plant Light-Harvesting Complex II: Linear Optical Spectra of Trimers and Aggregates. *Biochim. Biophys. Acta Bioenerg.* **2012**, *1817*, 1446 – 1460.

(43) Müh, F.; Madjet, M. E.-A.; Renger, T. Structure-Based Simulation of Linear Optical Spectra of the CP43 Core Antenna of Photosystem II. *Photosynth. Res.* **2012**, *111*, 87–101.

(44) Shibata, Y.; Nishi, S.; Kawakami, K.; Shen, J.-R.; Renger, T. Photosystem II Does Not Possess a Simple Excitation Energy Funnel: Time-Resolved Fluorescence Spectroscopy Meets Theory. *J. Am. Chem. Soc.* **2013**, *135*, 6903–6914.

(45) Lindorfer, D.; Müh, F.; Renger, T. Origin of Non-Conservative Circular Dichroism of the CP29 Antenna Complex of Photosystem II. *Phys. Chem. Chem. Phys.* **2017**, *19*, 7524–7536.

(46) Kitoh-Nishioka, H.; Yokogawa, D.; Irle, S. Förster Resonance Energy Transfer between Fluorescent Proteins: Efficient Transition Charge-Based Study. *J. Phys. Chem. C* **2017**, *121*, 4220–4238.

(47) Megow, J.; Renger, T.; May, V. Mixed Quantum-Classical Description of Excitation Energy Transfer in Supramolecular Complexes: Screening of the Excitonic Coupling. *ChemPhysChem* **2014**, *15*, 478–485.

(48) Madjet, M. E.-A.; Müh, F.; Renger, T. Deciphering the Influence of Short-Range Electronic Couplings on Optical Properties of Molecular Dimers: Application to "Special Pairs" in Photosynthesis. *J. Phys. Chem. B* **2009**, *113*, 12603–12614.

(49) Yin, S.; Dahlbom, M. G.; Canfield, P. J.; Hush, N. S.; Kobayashi, R.; Reimers, J. R. Assignment of the Qy Absorption Spectrum of Photosystem-I from Thermosynechococcus elongatus Based on CAM-B3LYP Calculations at the PW91-Optimized Protein Structure. *J. Phys. Chem. B* **2007**, *111*, 9923–9930.

(50) Hsu, C.-P.; You, Z.-Q.; Chen, H.-C. Characterization of the Short-Range Couplings in Excitation Energy Transfer. *J. Phys. Chem. C* **2008**, *112*, 1204–1212.

(51) Subotnik, J. E.; Cave, R. J.; Steele, R. P.; Shenvi, N. The initial and Final States of Electron and Energy Transfer Processes: Diabatization as Motivated by System-Solvent Interactions. *J. Chem. Phys.* **2009**, *130*, 234102.

(52) Vura-Weis, J.; Newton, M. D.; Wasielewski, M. R.; Subotnik, J. E. Characterizing the Locality of Diabatic States for Electronic Excitation Transfer By Decomposing the Diabatic Coupling. *J. Phys. Chem. C* **2010**, *114*, 20449–20460.

(53) Plasser, F.; Lischka, H. Analysis of Excitonic and Charge Transfer Interactions from Quantum Chemical Calculations. *J. Chem. Theory Comput.* **2012**, *8*, 2777–2789.

(54) Jordan, P.; Fromme, P.; Witt, H. T.; Klukas, O.; Saenger, W.; Krauß, N. Three-Dimensional Structure of Cyanobacterial Photosystem I at 2.5 Å Resolution. *Nature* **2001**, *411*, 909–917.

(55) Scholes, G. D. Long-Range Resonance Energy Transfer in Molecular Systems. *Annu. Rev. Phys. Chem.* **2003**, *54*, 57–87.

(56) König, C.; Neugebauer, J. Quantum Chemical Description of Absorption Properties and Excited-State Processes in Photosynthetic Systems. *ChemPhysChem* **2012**, *13*, 386–425.

(57) You, Z.-Q.; Hsu, C.-P. Theory and Calculation for the Electronic Coupling in Excitation Energy Transfer. *Int. J. Quant. Chem.* **2014**, *114*, 102–115.

(58) Cupellini, L.; Corbella, M.; Mennucci, B.; Curutchet, C. Electronic Energy Transfer in Biomacromolecules. *WIREs Comput. Mol. Sci.* **2019**, *9*, e1392.

(59) Knox, R. S.; Spring, B. Q. Dipole Strengths in the Chlorophylls. *Photochem. Photobiol.* **2003**, *77*, 497–501.

(60) Renger, T.; Madjet, M. E.; Müh, F.; Trostmann, I.; Schmitt, F.-J.; Theiss, C.; Paulsen, H.; Eichler, H. J.; Knorr, A.; Renger, G. Thermally Activated Superradi-

ance and Intersystem Crossing in the Water-Soluble Chlorophyll Binding Protein. *J. Phys. Chem. B* **2009**, *113*, 9948–9957.

(61) Becke, A. D. Density-Functional Thermochemistry. III. The Role of Exact Exchange. *J. Chem. Phys.* **1993**, *98*, 5648–5652.

(62) Grimme, S.; Ehrlich, S.; Goerigk, L. Effect of the Damping Function in Dispersion Corrected Density Functional Theory. *J. Comput. Chem.* **2011**, *32*, 1456–1465.

(63) Dunning Jr., T. H. Gaussian Basis Sets for Use in Correlated Molecular Calculations. I. The Atoms Boron through Neon and Hydrogen. *J. Chem. Phys.* **1989**, *90*, 1007–1023.

(64) Frisch, M. J.; Trucks, G. W.; Schlegel, H. B.; Scuseria, G. E.; Robb, M. A.; Cheeseman, J. R.; Scalmani, G.; Barone, V.; Mennucci, B.; Petersson, G. A. et al. Gaussian 09 Revision E01. Gaussian, Inc.: Wallingford, CT, 2009.

(65) Yanai, T.; Tew, D. P.; Handy, N. C. A New Hybrid Exchange-Correlation Functional Using the Coulomb-Attenuating Method (CAM-B3LYP). *Chem. Phys. Lett.* **2004**, *393*, 51 – 57.

(66) Schmidt, M. W.; Baldridge, K. K.; Boatz, J. A.; Elbert, S. T.; Gordon, M. S.; Jensen, J. H.; Koseki, S.; Matsunaga, N.; Nguyen, K. A.; Su, S. et al. General Atomic and Molecular Electronic Structure System. *J. Comput. Chem.* **1993**, *14*, 1347–1363.

(67) Singh, U. C.; Kollman, P. A. An Approach to Computing Electrostatic Charges for Molecules. *J. Comput. Chem.* **1984**, *5*, 129–145.

(68) Case, D. A.; Ben-Shalom, I. Y.; Brozell, S.; Cerutti, D.; Cheatham, III, T.; Cruzeiro, V. W. D.; Darden, T. A.; Duke, R. E.; Ghoreishi, D.; Gilson, M. K. et al. AMBER2018. University of California: San Francisco, 2018.

(69) Baker, N. A.; Sept, D.; Joseph, S.; Holst, M. J.; McCammon, J. A. Electrostatics of

Nanosystems: Application to Microtubules and the Ribosome. *Proc. Natl. Acad. Sci. USA* **2001**, *98*, 10037–10041.

(70) Morrison, A. F.; You, Z.-Q.; Herbert, J. M. Ab Initio Implementation of the Frenkel–Davydov Exciton Model: A Naturally Parallelizable Approach to Computing Collective Excitations in Crystals and Aggregates. *J. Chem. Theory and Comput.* **2014**, *10*, 5366–5376.

(71) Morrison, A. F.; Herbert, J. M. Low-Scaling Quantum Chemistry Approach to Excited-State Properties via an ab Initio Exciton Model: Application to Excitation Energy Transfer in a Self-Assembled Nanotube. *J. Phys. Chem. Lett.* **2015**, *6*, 4390–4396.

(72) Löwdin, P. On the Non- Orthogonality Problem Connected with the Use of Atomic Wave Functions in the Theory of Molecules and Crystals. *J. Chem. Phys.* **1950**, *18*, 365–375.

(73) Shao, Y.; Gan, Z.; Epifanovsky, E.; Gilbert, A. T.; Wormit, M.; Kussmann, J.; Lange, A. W.; Behn, A.; Deng, J.; Feng, X. et al. Advances in Molecular Quantum Chemistry Contained in the Q-Chem 4 Program Package. *Mol. Phys.* **2015**, *113*, 184–215.

(74) Head-Gordon, M.; Grana, A. M.; Maurice, D.; White, C. A. Analysis of Electronic Transitions as the Difference of Electron Attachment and Detachment Densities. *J. Phys. Chem.* **1995**, *99*, 14261–14270.

(75) Edmiston, C.; Ruedenberg, K. Localized Atomic and Molecular Orbitals. *Rev. Mod. Phys.* **1963**, *35*, 457–464.

(76) Plasser, F.; Wormit, M.; Dreuw, A. New Tools for the Systematic Analysis and Visualization of Electronic Excitations. I. Formalism. *J. Chem. Phys.* **2014**, *141*, 024106.

(77) Plasser, F.; Bäppler, S. A.; Wormit, M.; Dreuw, A. New Tools for the Systematic Analysis and Visualization of Electronic Excitations. II. Applications. *J. Chem. Phys.* **2014**, *141*, 024107.

(78) Becke, A. D. Density-Functional Exchange-Energy Approximation with Correct Asymptotic Behavior. *Phys. Rev. A* **1988**, *38*, 3098–3100.

(79) Lee, C.; Yang, W.; Parr, R. G. Development of the Colle-Salvetti Correlation-Energy Formula into a Functional of the Electron Density. *Phys. Rev. B* **1988**, *37*, 785–789.

(80) Iikura, H.; Tsuneda, T.; Yanai, T.; Hirao, K. A Long-Range Correction Scheme for Generalized-Gradient-Approximation Exchange Functionals. *J. Chem. Phys.* **2001**, *115*, 3540–3544.

(81) Tawada, Y.; Tsuneda, T.; Yanagisawa, S.; Yanai, T.; Hirao, K. A Long-Range-Corrected Time-Dependent Density Functional Theory. *J. Chem. Phys.* **2004**, *120*, 8425–8433.

(82) Hasegawa, J.; Ohkawa, K.; Nakatsuji, H. Excited States of the Photosynthetic Reaction Center of Rhodopseudomonas viridis: SAC-CI Study. *J. Phys. Chem. B* **1998**, *102*, 10410–10419.

(83) Reimers, J. R.; Cai, Z.-L.; Kobayashi, R.; Rästemp, M.; Freiberg, A.; Krausz, E. Assignment of the Q-Bands of the Chlorophylls: Coherence Loss via Qx - Qy Mixing. *Sci. Rep.* **2013**, *3*, 2761.

(84) Dreuw, A.; Head-Gordon, M. Failure of Time-Dependent Density Functional Theory for Long-Range Charge-Transfer Excited States: The Zincbacteriochlorin-Bacteriochlorin and Bacteriochlorophyll-Spheroidene Complexes. *J. Am. Chem. Soc.* **2004**, *126*, 4007–4016.

(85) MacKerell Jr., A. D.; Bashford, D.; Bellott, M.; Dunbrack Jr., R. L.; Evanseck, J. D.; Field, M. J.; Fischer, S.; Gao, J.; Guo, H.; Ha, S. et al. All-Atom Empirical Potential

for Molecular Modeling and Dynamics Studies of Proteins. *J. Phys. Chem. B* **1998**, *102*, 3586–3616.

(86) Suomivuori, C.-M.; Fliegl, H.; Starikov, E. B.; Balaban, T. S.; Kaila, V. R. I.; Sundholm, D. Absorption Shifts of Diastereotopically Ligated Chlorophyll Dimers of Photosystem I. *Phys. Chem. Chem. Phys.* **2019**, *21*, 6851–6858.

(87) Renger, T.; Müh, F. Understanding Photosynthetic Light-Harvesting: A Bottom up Theoretical Approach. *Phys. Chem. Chem. Phys.* **2013**, *15*, 3348–3371.

(88) Schrödinger, LLC, The PyMOL Molecular Graphics System, Version 1.8. 2015.

(89) Wang, X.; Ritschel, G.; Wüster, S.; Eisfeld, A. Open Quantum System Parameters for Light Harvesting Complexes from Molecular Dynamics. *Phys. Chem. Chem. Phys.* **2015**, *17*, 25629–25641.

(90) Cupellini, L.; Caprasecca, S.; Guido, C. A.; Müh, F.; Renger, T.; Mennucci, B. Coupling to Charge Transfer States is the Key to Modulate the Optical Bands for Efficient Light Harvesting in Purple Bacteria. *J. Phys. Chem. Lett.* **2018**, *9*, 6892–6899.

(91) Li, X.; Parrish, R. M.; Liu, F.; Kokkila Schumacher, S. I. L.; Martínez, T. J. An Ab Initio Exciton Model Including Charge-Transfer Excited States. *J. Chem. Theory Comput.* **2017**, *13*, 3493–3504.

Graphical TOC Entry